

UNIVERSITY OF OKLAHOMA
GRADUATE COLLEGE

THEORETICAL AND EXPERIMENTAL INVESTIGATION OF IV-VI MID-
INFRARED MULTIPLE QUANTUM WELLS VERTICAL CAVITY SURFACE
EMITTING LASERS

A Dissertation

SUBMITTED TO THE GRADUATE FACULTY

In partial fulfillment of the requirements for the

Degree of

Doctor of Philosophy

By

SHAHRIAR KHOSRAVANI
Norman, Oklahoma
2003

UMI Number: 3112346



UMI Microform 3112346

Copyright 2004 by ProQuest Information and Learning Company.

All rights reserved. This microform edition is protected against
unauthorized copying under Title 17, United States Code.

ProQuest Information and Learning Company
300 North Zeeb Road
PO Box 1346
Ann Arbor, MI 48106-1346

THEORETICAL AND EXPERIMENTAL INVESTIGATION OF IV-VI MID-
INFRARED MULTIPLE QUANTUM WELLS VERTICAL CAVITY SURFACE
EMITTING LASERS

A Dissertation APPROVED FOR THE
SCHOOL OF ELECTRICAL AND COMPUTER ENGINEERING

BY

Zhisheng Shi

Patrick J. McCann

James J. Sluss

Patrick L. Skubic

Bruce A. Mason

© Copyright by SHAHRIAR KHOSRAVANI 2003
All Rights Reserved

*Dedicated to my parents,
My late father, Abbas
and
My beloved mother, Shahin*

ACKNOWLEDGEMENT

I would like to express my gratitude to the following people. I start with my thesis advisor, Professor Zhisheng Shi, whose financial and technical support made this work possible. The next name that comes to my mind is Dr. Zhanming (Simon) Li, the president of Crosslight Software Inc., who generously sponsored collaboration with the University of Oklahoma during my employment. Despite its short period, this partnership was quite fruitful and resulted Chapters 3 and 4. I am also grateful to the research associate of the Electrical and Computer Engineering Department, Joe Grego, who eagerly shared tools and equipment wherever they were needed. During the experimental measurements, this work was also benefited by the assistance of my Optoelectronic group team members, including research associate Dr. Frank Zhao and graduate assistant Amitava Majumdar.

Finally, I greatly appreciate my beloved wife, Carol for her patient proofreading and editorial suggestions.

TABLE OF CONTENTS

CHAPTER 1

INTRODUCTION	1
1.1 Mid-Infrared Light	1
1.2 IV-VI Lead Salt Lasers	2
1.3 Vertical Cavity Surface Emitting Lasers (VCSELs)	4
1.4 VCSEL Structure	5
1.5 VCSEL Fabrication Methods	6
1.5.1 Etched air post	6
1.5.2 Ion implanted	7
1.5.3 Regrown buried heterostructure	7
1.5.4 Native oxide confinement	8
1.6 VCSEL Cavity	9
1.7 Distributed Bragg Reflector (DBR)	10
1.8 Development of an External Cavity Tunable Mid-Infrared VCSEL	13
References	14

CHAPTER 2

TEMPERATURE DEPENDENCY OF VCSEL OPERATION	17
2.1 Physical Model and Simulation Results	17
References	23

CHAPTER 3

OPTICAL MODE ANALYSIS OF VCSEL	25
3.1 Physical Model	25
3.2 Effective Refractive Index Method	25
3.3 Simulation Results	28
References	31

CHAPTER 4

BAND-GAP ENERGY SIMULATION USING EFFECTIVE MASS APPROXIMATION METHOD	32
4.1 Physical Model	32
4.2 Finite Difference Method	32
4.3 Simulation Results	36

References 40

CHAPTER 5

OPTICAL LOSS, QUANTUM EFFICENCY,
AND GAIN OF OPTICALLY PUMPED MID-INFRARED VCSEL 41

5.1 Measurement Techniques 41

5.2 Analysis 42

5.3 Experimental Results 45

References 50

CHAPTER 6

TE-COOLED OPTICALLY PUMPED
MID-INFRARED EXTERNAL CAVITY TUNABLE VCSEL 51

6.1 Optical Cavity Resonators 51

6.2 The Grating Equation 53

6.2.1 Resolving Power 58

6.3 Ray-Tracing Simulation of Diffraction Grating Linewidth,
A Demonstration of Linewidth Spot-Size Dependency 59

6.4 Tunable External Cavity Configurations 62

6.5 A New Type of External Cavity Configuration 63

6.6 Experimental Results 64

6.7 Analysis 66

References 69

CHAPTER 7

INSTRUMENTATIONS AND UTILITIES 70

7.1 OPTICAL DEVICES 70

7.1.1 Optical Steering Mechanism 70

7.1.2 Variable Angular Aperture 71

7.1.3 Optical Position/Angle Sensor With Angle Magnifier Mechanism
71

7.1.4 Double B/S Pseudo-Axial Optically Pumped T-Configuration 73

7.1.5 Far-Field Direct Measurement Apparatus 74

7.1.6 Calibration of Nd-YAG duty Cycle
by Measuring the Speed Of Light 75

7.1.7	Pseudo-Axial Optically Pumped Tunable External-Cavity Apparatus	76
7.2	ELECTRONIC DEVICES	78
7.2.1	PWM Controlled Peltier Driver	77
7.2.2	PZT Micro-position Driver	80
7.3	UTILITY SOFTWARE PACKAGES	82
7.3.1	Laser Line-width Dependency of Optical Absorption Spectrum	82
7.3.2	Far-field Optical Profile Simulation Using Monte-Carlo Method	83
7.3.3	VCSEL Reflectivity/Transmission Spectrum	85
	References	87
	SUMMARY	88
	APPENDIX:	
	BLACK BODY POWER CALIBRATION	89
	Theory of Black Body Radiation	89
	Optical Power Calibration Technique Using Black Body Reference Source	90
	MAPLE Pseudo-Code	93

CHAPTER 1: INTRODUCTION

1.1 Mid-Infrared Light

Mid-infrared section of the optical spectrum is typically between 3 to 30 μm wavelengths. This area represents optical absorption of a wide range of chemical and organic compounds. Mid-IR absorption spectroscopy is one of the known highly accurate chemical analyses. There are several requirements for the light source used in such techniques. Thermal stability, tunability, monochromaticity (i.e. spectral purity), and sufficient power output are a few vital elements of such a system. Considering all those factors plus portability, one can realize that there are not too many choices available today.

Lead salt lasers are one of the known sources for mid-infrared light. They can cover 2.9 to 27 μm wavelength. The main difficulty of lead salts is their poor thermal conductivity. This prevents the traditional edge-emitting laser to operate continuously (i.e. CW mode) at room temperature. CW mode is a necessary condition, since any spectral analysis needs a light source with minimum harmonics. To this date, the highest temperature CW mid-IR available is around 223K, which is still well below thermoelectric cooling range (i.e.~260K).

The main goal of this research is to assist the development of an innovative light source that can be installed in a portable optical spectroscopy unit. In order to achieve such a goal, we need to increase the operating temperature to at least the thermoelectric (Peltier) range. Based on our previous studies and simulationsⁱ an innovative lead salt vertical-cavity surface-emitting laser could operate at 282K in CW mode. Room temperature CW operation could be achieved if one can reduce the nonradiative recombination processes,

mainly Auger coefficient by one order of magnitude. We believe this is feasible since a quantum well design of such system has intrinsic advantage to a bulk. After we reported the first Pb-salt VCSELs^{ii,iii}, significant progresses have been made in developing QW VCSELs^{iv}. Our recent experiments on quantum well vertical cavity surface emitting laser (QW VCSEL), PbSe based confirmed above-room-temperature pulse mode laser emission^v.

1.2 IV-VI Lead Salt Lasers

Lasers with direct band-to-band transitions using IV-VI lead salts^{vi,vii} have been commercially available for many years. They hold the highest electrically pumped CW operation temperature 223K at wavelengths longer than 3 μm . Strong enhancement of the Auger non-radiative lifetime has been the main advantage of these materials in the long wavelength regime. While Auger processes are the primary mechanism responsible for the rapid degradation of III-V interband semiconductor laser performance with increasing wavelength, it is well known that the Auger coefficient (γ_3) in IV-VI structures^{viii,ix} is more than an order of magnitude lower than those in type-II QWs^x. In addition, bandgap energies of IV-VI semiconductors increase strongly with temperature, providing advantages of wide temperature and current tuning ranges. The increase of the IV-VI bandgap energy with increasing temperature also helps reduce facet heating and therefore increases laser reliability at high temperatures and high output power. This is a great disadvantage of III-V lasers, which are known to suffer from thermal runaway problems associated with a decrease in bandgap energy as temperature increases^{xi}. There has often been a misunderstanding that IV-VI lasers cannot produce high output power. In fact, it has been reported that even a diffused-junction laser can produce up to 24mW of CW

output^{xii}. Low thermal conductivity of IV-VI materials however, prevents room temperature CW operation of traditional IV-VI lasers. Due to their relatively long wavelength, mid-IR diode lasers also have a large diffraction angle. In addition to the extended large far field, standard DH-lasers have multimode emission caused by their poor-defined stripe contact active volume. Consequently, the resulting far fields show sporadic shape plus temperature and current dependency.

Degeneracy of the L-valley conduction and valence band extrema significantly increases the lasing threshold of lead salts by four-fold. Quantum confinement does not lift the degeneracy in edge-emitting QW devices, since the four valleys remain symmetric for the (100) growth that must be employed to allow for the cleaving of laser cavities. Even with the threshold reduction that comes from a low non-radiative recombination, which is perhaps the greatest advantage of IV-VI laser materials for high-temperature and long-wavelength operation, their poor thermal conductivity is the main obstacle of full development of IV-VI material systems.

Lead salt vertical-cavity surface-emitting lasers' (VCSELs) performance surpass many of the main limitations of IV-VI edge-emitters, and once optimized should provide a superb high-temperature, single-mode, CW source for spectroscopy and other mid-IR applications. First, the short vertical cavity, when combined with a small lateral dimension on the order of 1-3 wavelengths, should produce a spatially stable single-mode output of high spectral purity. Second, since no cleaving is required, the laser structures may be grown on (111) BaF₂ substrates, which for many years have been used routinely to fabricate high-quality non-laser IV-VI structures^{xiii}. Besides taking advantage of five-fold enhancement of the room-temperature thermal conductivity in BaF₂ over that in

PbSe, this configuration will allow the growth of QW VCSELs in which the degeneracy of the L valleys is lifted. The reduction of the threshold carrier concentration by up to four-fold should make room-temperature CW operation quite feasible. The efficiency may also be improved significantly, mainly for two reasons. First, the free carrier absorption losses are reduced. Then, much shorter effective cavity length in a VCSEL allows a larger fraction of the mid-IR light to be emitted before it is reabsorbed.

1.3 Vertical Cavity Surface Emitting Lasers (VCSELs)

The vertical cavity surface emitting laser has many potential advantages over the edge-emitting lasers. Circular output beam with high spectral purity and coherence, and high two-dimensional (2-D) packing density for arrays are important characteristics of VCSEL. Its design allows the chips to be manufactured and tested on a single wafer. Large arrays of devices can be created exploiting methods such as 'flip' chip optical interconnects and optical neural network applications. In the telecommunications industry, the VCSEL uniform, single mode beam profile is desirable for coupling into optical fibers. Since the VCSEL has an ultra low cavity length ($\sim 1\text{-}3\mu\text{m}$), it can lase in single longitudinal and lateral modes. Nevertheless, the maximum single-mode power attainable is limited by the start of higher order lateral-mode emission. With the increase of injection current or optical pumping power, the VCSEL operates in a single longitudinal but multiple lateral modes.

The earliest VCSEL was reported in 1965 by Melngailis^{xiv}. It consisted of a n^+pp^+ junction of InSb. The device emitted coherent radiation at a wavelength of around $5.2\ \mu\text{m}$ when it was cooled to $10\ \text{K}$ and subjected to a magnetic field in order to confine the carriers. Later, other groups reported on the grating surface emission^{xv}, near infrared

emission close to telecommunications wavelength of $1.5\ \mu\text{m}$. This was achieved by Iga, Soda, et al in 1979^{xvi} at the Tokyo Institute of Technology. These early VCSEL devices had metallic mirrors with resulting high threshold current densities (44KAcm^{-2}) and were cooled using liquid nitrogen. Epitaxial mirrors for GaAs/AlGaAs VCSELs were pioneered in 1983^{xvii}. A year later^{xviii}, pulsed room temperature VCSELs were produced in the laboratory. Reduction in the active volume of the cavity was the main cause of reduction in the threshold current density. GaAs/AlGaAs VCSELs with native oxide current confinement structure have achieved threshold currents as low as $40\mu\text{A}$ ^{xix}.

1.4 VCSEL Structure

There are many designs of the VCSEL structure. However, they all have certain aspects in common. The cavity length of a VCSEL is very short, typically 1-3 wavelengths of the emitted light. As a result, in a single pass of the cavity a photon has a small chance of triggering a stimulated emission event at low carrier densities. Therefore, VCSELs require highly reflective mirrors to be efficient. In edge-emitting lasers, the reflectivity of the facets is about 30%. For VCSELs, the reflectivity required for low threshold currents is greater than 99.9%. Such a high reflectivity cannot be achieved by the use of metallic mirrors. VCSELs make use of Distributed Bragg Reflectors (DBRs). These are formed by laying down alternating layers of semiconductor or dielectric materials with a difference in refractive index. Since the DBR layers also carry the current in the device, more layers increase the resistance of the device. Therefore heat dissipation and growth may become a problem if the device is poorly designed.

1.5 VCSEL Fabrication Methods^{xx}

The most common VCSEL fabrication methods can be categorized in four groups. Each has its pros and cons. The following are brief descriptions of each category.

1.5.1 Etched air post

Fig. 1.2 shows the etched air-post, which was the first monolithic electrically pumped VCSEL^{xxi}.

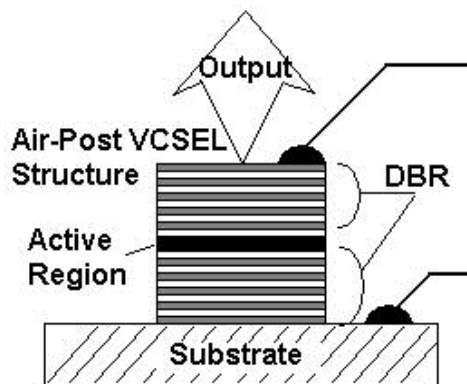


Fig. 1.2) Air-Post VCSEL structure

Injected carriers are forced to travel down the narrow pillar, yielding a high current density. The refractive index transition between the pillar material and the surrounding air acts as a waveguide for the radiation, confining it to the active region. This approach has suffered from a number of problems. Scattering loss from the side-walls, excess free carrier absorption at the side-walls, high ohmic resistance, poor reliability due to exposed active surface and poor heat dissipation of the structure are the main shortcomings of this approach. The latter has been improved through immersion in material with high thermal conductivity^{xxii}. Since there is a wide lateral step, the waveguide can easily become multimode, unless the lateral dimension is reduced. This is disadvantageous for applications (i.e. spectroscopy) requiring large, single-mode powers.

1.5.2 Ion implanted

VCSEL is fabricated using energetic protons to bombard the top DBR of the structure, destroying its electrical conductivity in selected areas (Fig. 1.3).

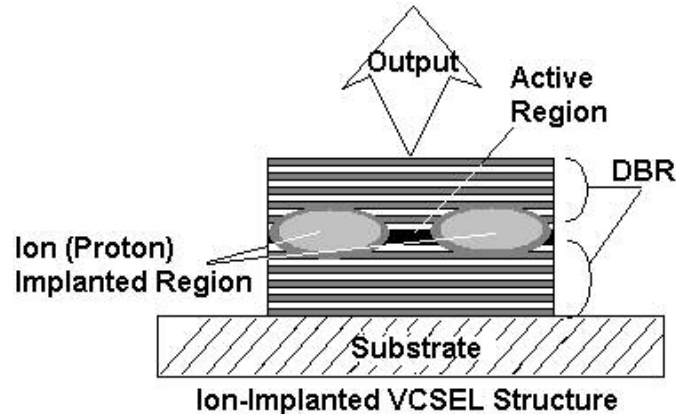


Fig. 1.3

As a result, the carriers are funneled into the gap defining the active region. However, the ion implantation is fuzzy at the edges and causes crystal damage in the active region, making it very difficult to define very small structures.

There is no built-in waveguiding in a proton implanted VCSEL, but localized heating at the injected region induces a thermal lens by changing the refracting index. Therefore waveguiding is difficult, as the beam direction and divergence change with the temperature.

1.5.3 Regrown buried heterostructure

A similar structure to the air post is shown in Fig. 1.4. A pillar is etched as before, but now the gaps surrounding the pillar are filled with a semiconductor of larger band-gap. The regrown material provides electrical and optical confinement, as the refractive index is lower. The regrown region can also conduct heat away from the active region, and as

the index is higher than that of air, the VCSEL can stay single-mode for longer in comparison with a simple air-post. All these benefits are made at the expense of more

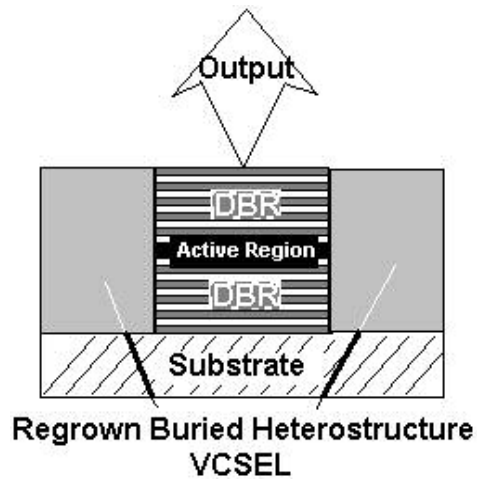


Fig. 1.4

complicated processing, which limits the usefulness of the technique in a manufacturing context.

1.5.4 Native oxide confinement

The most promising technology for defining the active region is provided by the use of oxidized confinement layers (Fig. 1.5). This technique makes use of the fact that AlGaAs layers with very high (>95%) aluminum content will oxidize when exposed to water vapor at high temperatures^{xxiii,xxiv}. The resulting dielectric oxide has an abrupt oxidation edge.

This means that very small active regions are feasible. Optical confinement is an additional advantage, which is provided by the low refractive index dielectric layer. A drawback of this technique is that the oxidation rate is very sensitive to the *Al* content in the oxidizing layer, a factor that may become a disadvantage in a manufacturing process.

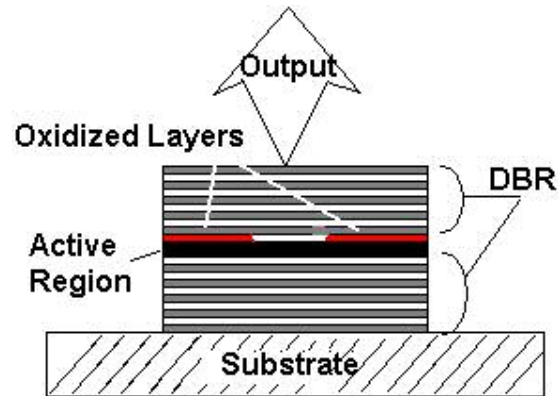


Fig. 1.5

VCSELs fabricated with this technique have demonstrated efficiencies $\sim 50\%$, threshold currents $< 50\mu\text{A}$ and modulation bandwidths $\sim 20\text{GHz}^{\text{xxv}}$.

1.6 VCSEL Cavity

In today's technology, most VCSEL devices employ quantum wells within the active region. By depositing a thin layer of semiconductor with a slightly smaller band gap, one can not only define a region for recombination to occur, but also control the optical properties of the device.

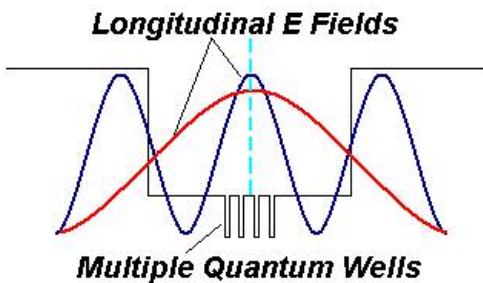


Fig. 1.6) Quantum wells are positioned at antinodes of E field.

Discrete energy levels are formed in the conduction and valence bands. Transitions from the conduction band to valence band energy levels occur from states that have the same value of n quantum number. The power obtained from a single quantum well is low.

Multiple quantum wells may be grown within the cavity to increase output power. The position of the quantum wells is crucial. To maximize the gain of the device, quantum wells should be positioned at antinodes of the E field standing wave inside the cavity (Fig. 1.6). This can directly determine the optical confinement factor discussed in more detail in chapter 5.

1.7 Distributed Bragg Reflector (DBR)

The reduced cavity length in VCSELs and the addition of quantum wells significantly reduces the probability of stimulated emission in a single pass of the cavity. The light within the cavity must be reflected back into the cavity many more times than with a Fabry-Perot edge emitter laser.

The average time the photons spend within the cavity is known as the photon lifetime. The reflectivity of the mirrors must be very high to increase the photon lifetime and consequently increase the interaction time with electrons in the excited states (i.e. stimulated emission). Threshold gain occurs where the optical gain equals the total optical loss. At the gain threshold, we have

$$R_1 R_2 e^{2(g_{th} \cdot L_{QW} - \alpha \cdot L_{cav})} = 1 \quad (1.1)$$

Expressed in terms of the gain:

$$g_{th} = \frac{1}{2L_{QW}} \left[Ln \frac{1}{R_1 R_2} + \alpha L_{cav} \right] \quad (1.2)$$

Where α is the absorption coefficient, L_{QW} and L_{cav} are the lengths of the gain region and the quantum well respectively. R_1 and R_2 are the mirror reflectivities. Let's assume an

ideal device with no absorption. Let $R_1=R_2=R$. Gain of 1000cm^{-1} gives a mirror reflectivity of 99.95%. Metallic mirrors are limited to a reflectivity of $\sim 98\%$. Thus they are useless for such small active regions. Dielectric materials and semiconductors have a very low absorption coefficient for photons with energies below their bandgap energy. If two dielectric materials with different refractive indices are placed together to form a junction, light will be reflected at the interface.

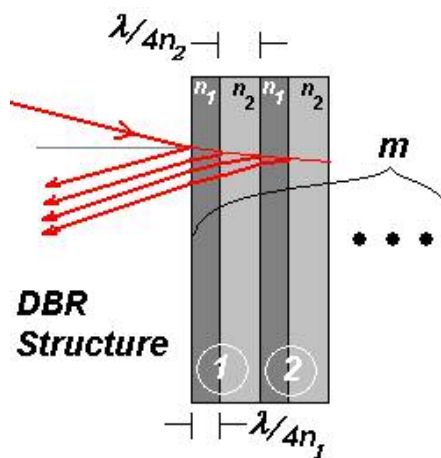


Fig. 1.7) Schematic diagram of a DBR with m repeated dielectric pairs

The amount of reflected light from one such boundary is small. However, if layers of alternating semiconductor or dielectric are stacked periodically, where each layer has an optical thickness $\lambda/4n$, the reflections from each of the boundaries will be added in phase to produce a large reflection coefficient (Fig. 1.7 and 1.8). The number of layers required to produce a highly reflective mirror at a particular wavelength is determined by the difference in the refractive index of the contrasting materials. In order to avoid failure caused by strain effects, it is crucial that the difference of lattice constant of the materials at each interface must be within about one percent. Given the refractive index of the

substrate n_s and surrounding material (usually air) n_0 , as well as the refractive indices of the contrasting semiconductors n_1, n_2 for a given period m , the reflectivity is given by^{xxvi}:

$$R = \left[\frac{1 - \frac{n_s}{n_0} \left(\frac{n_1}{n_2} \right)^{2m}}{1 + \frac{n_s}{n_0} \left(\frac{n_1}{n_2} \right)^{2m}} \right]^2 \quad (1.3)$$

Mirrors for long-wavelength devices must be designed carefully, arranging a number of parameters.

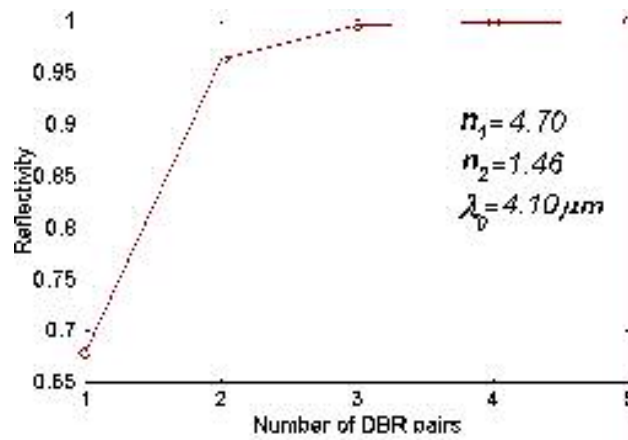


Fig. 1.8) Reflectivity of $Pb_{0.65}Sr_{0.35}Se/BaF_2$ alternating quarter-wavelength mirror stacks as a function of the number of mirror pairs

The most important considerations relate to the choice of materials used to fabricate the Bragg layers⁵. These must be grown using materials that lattice-match to the material of the device cavity. Each layer of semiconductor increases the resistance of the device and raises the threshold current, so it is important to minimize the number of layers required. Growing such Bragg reflectors puts considerable demands on the fabrication process and creates random reliability. Nevertheless, highly reflective DBR mirrors can be fabricated from dielectric materials.

1.9 Development of an External Cavity Tunable Mid-Infrared VCSEL

Tunable mid-infrared lasers are the critical element of any laser absorption spectroscopy. The current available IV-VI devices in the market are all cryogenic ($T \sim 77\text{K}$) and the operating temperature and the bias current are the main controls of the laser tuning. The fabrication of a room temperature CW mid-infrared laser has been a goal of many research groups around the world. The experimental results of the mid-infrared VCSELs developed at the University of Oklahoma have shown to be promising toward such a goal. However, poor thermal conduction of IV-VI material system is the main obstacle for the CW room temperature operation.

The limitations of VCSEL tuning (due to its short cavity) and its low heat dissipation characteristic demand for an alternative approach.

The proposed method is to fabricate a VCSEL without the top DBR mirror and use an external cavity instead. This design simultaneously provides two major advantages. First, the removal of thermally resistive DBR allows a direct heat-sink contact to the active region; therefore, the highest heat dissipation possible can be expected. Second, the missing DBR can be substituted by an optical grating. This not only provides the end mirror needed to form a cavity, but also provides a simple and versatile tuning mechanism. Chapter 6 gives a detail description of the working prototype.

REFERENCES:

-
- ⁱ S. Khosravani, Z. Shi "Theoretical investigation of IV-VI mid infrared Vertical Cavity Surface Emitting Lasers" Applied Physics Letters January 8, 2001
- ⁱⁱ Z. Shi, G. Xu, P.J. McCann, and X. M. Fang, N. Dai, C. L. Felix, W. W. Bewley, I. Vurgaftman, and J. R. Meyer, MRS 1999 Fall meeting, Nov. 30, 1999, Boston Massachusetts.
- ⁱⁱⁱ Z. Shi, G. Xu, P. J. McCann, X. M. Fang, N. Dai, C. L. Felix, W. W. Bewley, I. Vurgaftman, and J. R. Meyer, Appl. Phys. Lett. 76, 3688 (2000).
- ^{iv} C. L. Felix, W. W. Bewley, I. Vurgaftman, J. R. Lindle, J. R. Meyer, H. Z. Wu, G. Xu, S. Khosravani, and Z. Shi, Appl. Phys. Lett. 78, 3770 (2001).
- ^v F. Zhao, H. Wu, L. Jayasinghe and Z. Shi, "Above-room-temperature optically pumped 4.12 μm mid-infrared vertical-cavity surface-emitting lasers", submitted to Applied Physics Letters
- ^{vi} Z. Feit, M. McDonald, R.J. Woods, V. Archambault and P. Mak, "Low threshold PbEuSeTe/PbTe separate confinement buried heterostructure diode lasers", Appl. Phys. Lett. **68**, 738(1996).
- ^{vii} U. P. Schliessl and J. Rohr, Infr. Phys. Tech. 40, 325 (1999)
- ^{viii} R. Klann, T. Hofer, R. Buhleier, T. Elsaesser, and J. W. Tomm, J. Appl. Phys. 77, 277 (1995).
- ^{ix} P C Findlay, C R Pidgeon, B N Murdin, A F G van der Meer, A F G Langerak, C M Ciesla, J Oswald, G Springholz and G Bauer, "Suppression of non-radiative scattering processes in narrow gap semiconductors", Phys. Rev. **B58**, 12908 (1998).
- ^x J. R. Meyer, C. L. Felix, W. W. Bewley, I. Vurgaftman, E. H. Aifer, L. J. Olafsen, J. R. Lindle, C. A. Hoffman, M.-J. Yang, B. R. Bennett, B. V. Shanabrook, H. Lee, C.-H. Lin, S. S. Pei, and R. H. Miles, Appl. Phys. Lett. 73, 2857 (1998).
- ^{xi} Hong H. Lee, "Effect of lateral heat and carrier diffusion on thermal runaway of cw DH semiconductor lasers", IEEE J. Quantum Electron, **29**, 2619(1993)
- ^{xii} Laser Focus World Jan. 9(1997)

-
- ^{xiii} G. Springholz, Z. Shi and H. Zogg, *Thin Films: Heteroepitaxial: Systems*, Eds. W. K. Liu, & M. B. Santos, World Scientific, 1999
- ^{xiv} I. Melngailis, Longitudinal injection-plasma laser of InSb, *Applied Physics Letters*, 6, No.3, pp 59-60. (1965)
- ^{xv} R. D. Burnham, D. R. Scifres, and W. Striefer, Single-heterostructure distributed feedback GaAs diode lasers, *IEEE J. Quant. Elec.* QE-11 pp 439-449 (1975)
- ^{xvi}] H. Soda, K. Iga, C. Kitahara and Y. Suematsu, GaInAsP/InP Surface Emitting Injection Lasers, *Jpn. J. Appl. Phys.* 18, pp 2329-2330 (1979)
- ^{xvii} H. Soda, K. Iga, C. Kitahara and Y. Suematsu, GaInAsP/InP Surface Emitting Injection Lasers, *Jpn. J. Appl. Phys.* 18, pp 2329-2330 (1979)
- ^{xviii} A. Chailertvanitkul, S. Uchiyama, Y. Kotaki, Y. Kokobun and K. Iga, Annual Meet. *Jpn. Soc. Appl. Phys.* Tokyo, Japan (1983)
- ^{xix} I. Ibaraki, S. Ishikawa, S. Ohkouchi and K. Iga, *Elec. Letts.* 20 pp 420 (1984).
- ^{xx} *Vertical Cavity Surface Emitting Lasers, Design, Fabrication, Characterization and Applications*, By: C. Wilmsen, H. Temkin and L.A. Coldren, Cambridge University Press 1999, pp. 2-12
- ^{xxi} J. L. Jewell, A. Sherer, S. L. McCall, Y. H. Lee, S. Walker, J. P. Harbison and L. T. Florez, Low-threshold electrically pumped vertical-cavity surface-emitting microlasers, *Electron. Lett.*, 25, 1123 (1989).
- ^{xxii} K. D. Choquette, G. Hasnain, J. P. Mannaerts, J. D. Wynn, R. C. Wetzel, M. Hong, R. S. Freund and R. E. Leibenguth, Vertical-cavity surface-emitting lasers fabricated by vacuum integrated processing, *IEEE Photonics Technol. Lett.*, PTL-4, 951-954 (1992).
- ^{xxiii} W. T. Tsang, Self-terminating thermal oxidation of AlAs epilayers grown on GaAs by molecular beam epitaxy, *Appl. Phys. Lett.*, 33, 426 (1978).
- ^{xxiv} J. M. Dallesasse, N. Holonyak, Jr., A. R. Sugg, T. A. Richard and N. El-Zein, Hydrolysis oxidation of $\text{Al}_x\text{Ga}_{1-x}\text{As}$ -AlAs-GaAs quantum well heterostructures and superlattices, *Appl. Phys. Lett.*, 57, 2844 (1990).
- ^{xxv} K. L. Lear, K. D. Choquette, R.P. Schneider Jr., S. P. Kilcoyne and K. M. Geib, Selectively oxidised vertical-cavity surface emitting lasers with 50% power conversion efficiency, *Electron. Lett.*, 31, 208 (1995).

^{xxvi} Vertical Cavity Surface Emitting Lasers, Design, Fabrication, Characterization and Applications, By: C. Wilmsen, H. Temkin and L.A. Coldren, Cambridge University Press 1999, pp. 34-40

CHAPTER 2: TEMPERATURE DEPENDENCY OF VCSEL OPERATION^{xxvii}

Laser performance requirements that are not yet available include continuous wave (CW) operation at room temperature (or at least the thermoelectric cooling range of $T > 240\text{K}$), spectral purity and reasonable output power ($> 1\text{mW}$) with good beam quality. Currently, IV-VI lead salts^{xxvii, xxvii, xxvii} quantum cascade^{xxvii, xxvii} and type-II quantum well (QW) diode lasers^{xxvii, xxvii, xxvii} are leading approaches being pursued to meet these application needs. Auger recombination is the main loss channel for all band-to-band mid-IR laser materials at high temperature. Auger coefficients of IV-VI materials are typically an order of magnitude smaller^{xxvii, xxvii} than those in type-II QW lasers.

These in turn are significantly suppressed relative to other III-V and II-VI semiconductors with the same energy gaps^{xxvii}. This is perhaps the greatest advantage of IV-VI laser materials for high-temperature and long-wavelength operation. The major drawback of IV-VI materials is low thermal conductivity. Recently, we have reported optically pumped IV-VI mid-IR vertical-cavity surface emitting lasers (VCSELs) that operated at 289K in pulse mode^{xxvii, xxvii, xxvii}. Lead salt VCSELs may overcome many of the main limitations of IV-VI edge-emitters as described in Ref. 15. Once optimized, this should provide an attractive high-temperature, single-mode CW source for spectroscopy and other mid-IR applications. Theoretical investigation on such lasers will be of great interest to help understand the impact of Auger recombination and heat dissipation.

The core of simulation presented here is the simultaneous solution of the coupled rate Eqs. (1)–(3) given by^{xxvii}

$$\frac{dN}{dt} = \frac{P}{Ad\hbar\omega_{pump}} - \gamma_3(T_l)N^3 - R_{sp}(N, T_l) - \frac{N}{\tau_{SR}} - \sum_m \Gamma_m \frac{c}{n_m} g(\hbar\omega, N, T_l) \frac{S_m}{A} \quad (2.1)$$

$$\frac{dS_m}{dt} = \beta AR_{sp}(N, T_l) + \frac{c}{n_m} \left(\Gamma_m g - (1 - \Gamma_m) \alpha_{clad} - \Gamma_m \sigma_F N + \frac{\ln(R_1 R_2)}{2L_{cav}} \right) S_m \quad (2.2)$$

$$T_l \approx T_l^0 + \left[\frac{(E_e^{inj} + E_h^{inj}) \frac{P}{Ad\hbar\omega_{pump}} + d\gamma_3 N^3 E_g}{+ \sum_m \hbar\omega_m \frac{c}{n_m} ((1 - \Gamma_m) \alpha_{clad} + \Gamma_m \sigma_F N) \frac{S_m}{w}} \right] \frac{d_{HS}}{\kappa_{\perp}} \quad (2.3)$$

where N is carrier concentration density, P is pumping power, d is the active region thickness, $\hbar\omega_{pump}$ is photon energy of the pump, T_l is lattice temperature, γ_3 is the Auger coefficient taken from reference¹⁰, R_{sp} is spontaneous radiation rate estimated from the typical measured spontaneous power of PbSe DH lasers^{xxvii}, τ_{SR} (~ 10 nsec) is the Shockley– Read lifetime, A is the effective active region area (i.e., circular opening with radius $\sim 30\mu m$), mode m (throughout the calculation, single mode operation is assumed. i.e., $m = 1$), mode refractive index n_m , g is the gain based on the expression provided by Reference^{xxvii}. R_1 and R_2 are the bottom and top mirror reflectivity with $R_1 = 0.994$, $R_2 = 0.93$.

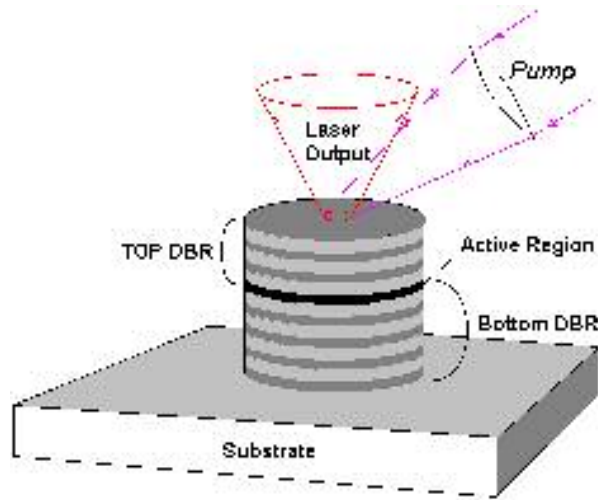


Fig. 2.1) Optically pumped VCSEL Structure

The reflectivity was calculated for a three-pair bottom mirror and a two-pair top mirror described in Reference¹⁵. In Eq. (2.2), only free carrier absorption is considered as a loss term. Other possible losses such as interface recombination were ignored. Note that Joule heating in Eq. (2.3) is eliminated due to optical pumping.

Standard Runge–Kutta method with 10^{-4} relative error was used. The steady-state values for the carrier density, photo density and lattice temperature are obtained once transient relaxation oscillations have faded out. Lattice temperature instead of electron temperature at steady states in Eqs. (2.1) and (2.2) was used, since there is only a minute difference between the two. Equation (2.3) is basically the linear approximation of thermal conductivity. In order to couple Eq. (2.3) to the others, its first time derivative was calculated as our time dependent lattice temperature equation.

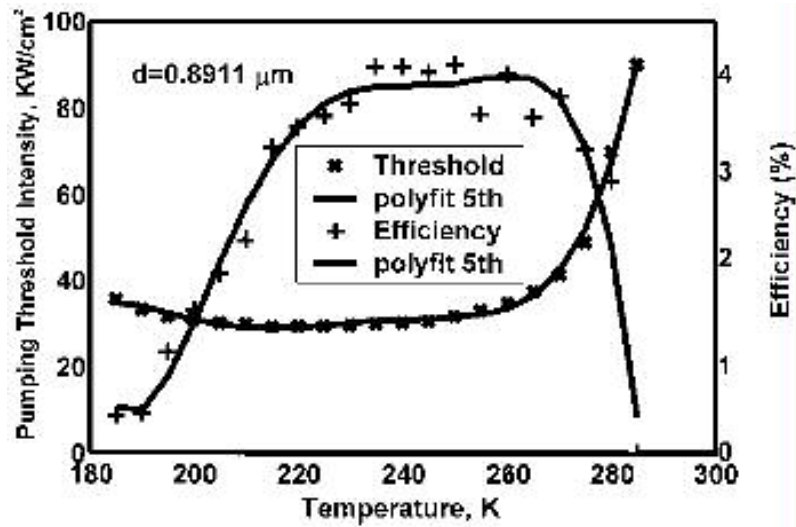


Fig. 2.2) Simulated efficiency and pumping threshold intensity for optimized cavity thickness $d = 2.098 \mu\text{m}$

This simplifies Eq. (2.3) and gives slower and smoother temperature variation without losing the accuracy of the equations. The VCSEL structure used for our calculation is shown in Fig. 2.1. The cavity thickness was chosen so that the maximum overlap of the cavity mode with the gain peak would occur at a desired temperature. The design of the top DBR mirror was intended to place the pump wavelength of $2.098 \mu\text{m}$ in a low-ripple region of the reflectivity interference fringes. We note that the energy gap of the $\text{Pb}_{0.85}\text{Sr}_{0.15}\text{Se}$ on the top DBR is larger than the pump photon energy.

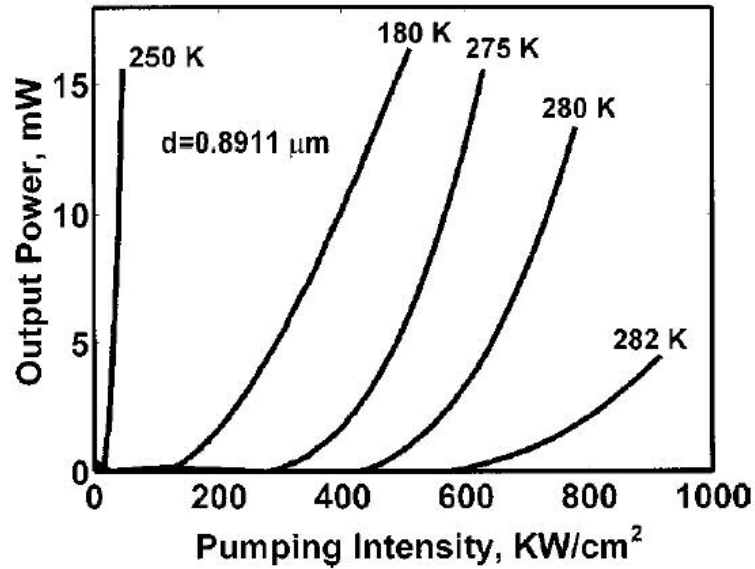


Fig. 2.3) VCSEL output power vs. pump intensity at five temperatures, for a circular pump spot with radius $r = 30 \mu\text{m}$

Based on our simulation of top mirror reflectivity for 37° incident light at $2.098 \mu\text{m}$ about 80% of the pumping energy would be absorbed in the active region. Considering thermo-electrical cooling limit (i.e., 250K) and thermal runaway predicted by our simulation for $T > 255\text{K}$, an optimized thickness for $T = 250\text{K}$ was obtained through the following procedure. Gain equation was first solved for several different values of carrier concentration density N . Maximum gain was then calculated for the average asymptotic value of N . From the maximum gain profile $\hbar\omega$ and consequently λ and d were obtained ($\lambda = n_m d$). Finally, the thickness d ($0.8911 \mu\text{m}$) was used to calculate the threshold and efficiency over a range of temperatures starting at 180K. Fig. 2.2 plots the dependencies of both the threshold pump intensity and the optical power conversion

efficiency on temperature. In this plot, each individual data point is produced by separate simulation. Fig. 2.3 shows the light–light curves at the series of temperatures.

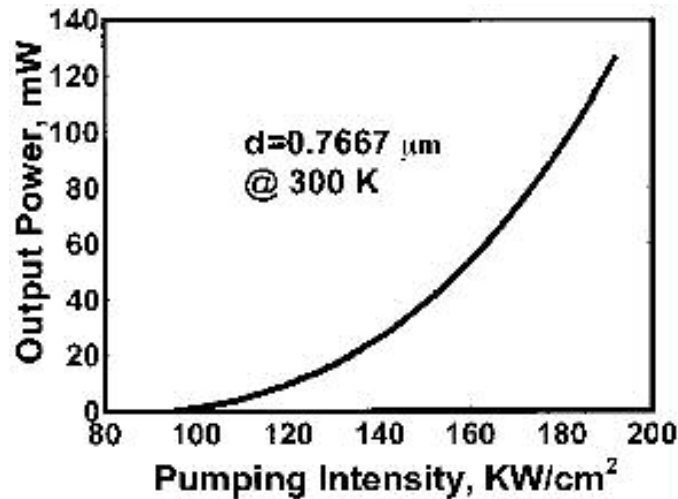


Fig. 2.4) Output power vs. pump intensity for the lead salt VCSEL at room temperature with sufficient heat dissipation.

As can be seen from Fig. 2.3 optimization for $T=250\text{K}$ results lower output and higher threshold for $T<250\text{K}$ or $T>250\text{K}$. Although the output power and efficiency are higher than their experimental values, the locations of the threshold pumping and the shape of temperature dependent efficiency agree well with the reported experimental data¹³⁻¹⁵. The reason for higher simulated output power might be due to the fact that all other loss terms such as interface recombination in Eq. (2.2) were not included. We note that more loss terms in Eq. (2), or even shorter Shockley–Read lifetime in Eq. (2.1), will reduce the efficiency and the output power but they do not prevent the VCSEL from lasing. The dominating loss term here is the fast Auger recombination process. To investigate the impact of Auger recombination and the heat dissipation separately, Eq. (2.3) was ignored in order to prevent thermal runaway. Thickness d was also optimized through the previous procedure for 300K . As shown in Fig. 2.4 the Auger recombination does not

prevent the IV-VI VCSELs from operating at room temperature in CW mode if the generated heat can be efficiently removed from the active region.

Auger recombination is the dominating loss channel and determines the heat generation for all IV-VI diode lasers. Therefore, this result can also be applied to all IV-VI diode lasers, which have a similar gain and loss ratio including the edge-emitting laser. Our simulation showed that reduction of Auger recombination $\gamma_3 N^3$ by an order of magnitude either by reducing the Auger coefficient γ_3 or by reducing threshold carrier concentration N (note that the effect is $\propto N^3$) will allow room temperature CW operation of the same VCSEL structure even with heat dissipation. Since the threshold carrier concentration in PbSe QW laser structures could be reduced¹⁹ and likely Auger coefficient as well, PbSe QW VCSELs should be able to operate at room temperature in CW mode.

REFERENCES:

CHAPTER 3: OPTICAL MODE ANALYSIS OF VCSEL

3.1 Physical Model

Optical mode analysis is a very important aspect of any dynamical model of a VCSEL.

Since a VCSEL has a very short cavity, one can expect only one allowed longitudinal mode. However, the width of VCSEL pillar might allow multilateral mode lasing. There are two major reasons to have these modes reduced. First, the performance of a laser can be simply measured by its linewidth, where the large linewidth represents a large number of lasing modes. (In the case of a VCSEL, this translates to multilateral modes.) Second,

having a multimode laser directly translates to a lower efficiency, since the pumping energy has to energize many undesired modes. Therefore, lowering the allowed optical modes of a laser is a primary concern during its design process.

3.2 Effective Refractive Index Method

The concept of effective refractive index method^{xxvii} relies on a basic approximation.

Let's assume a simple VCSEL structure. The structure is composed of a pillar, stacked on a substrate layer with low aspect ratio (i.e. pancake shape). (Fig. 3.1)

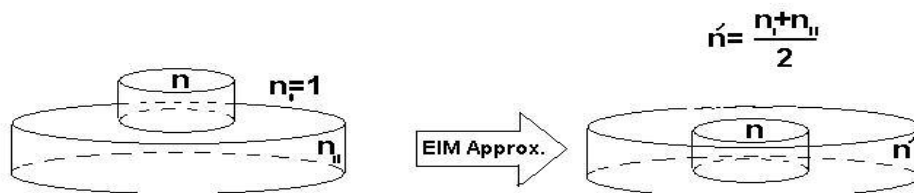


Fig. 3.1) Effective refractive index method illustration

For simplicity let's assume the structure has a cylindrical symmetry (i.e. no ϕ dependency). One can substitute it with a single fused layer, which is composed of an inner core with the same refractive index as the pillar surrounded by a layer whose refractive index is the average of the refractive index of air and substrate respectively.

This in turn greatly reduces the complexity of the calculation. Using classical electromagnetic theory, one can solve this boundary value problem. Let's start with Maxwell's equations. In an infinite medium, the electric and magnetic field can be

defined by the following equations^{xxvii},

$$\begin{aligned} \nabla \cdot E &= 0 & \nabla \times E + \frac{1}{c} \frac{\partial B}{\partial t} &= 0 \\ \nabla \cdot B &= 0 & \nabla \times B - \frac{\mu \epsilon}{c} \frac{\partial E}{\partial t} &= 0 \end{aligned} \quad (3.1)$$

where the medium is characterized by the parameters μ , ϵ . By combining the two curl equations and writing the Cartesian component of E and B separately, one can find that each satisfies the wave equation,

$$\nabla^2 W - \frac{1}{v^2} \frac{\partial^2 W}{\partial t^2} = 0 \quad (3.2)$$

and

$$v = \frac{c}{\sqrt{\mu \epsilon}} \quad \text{or} \quad v = \frac{c}{n} \quad (3.3)$$

where n is the refractive index of the medium. In case of a VCSEL, one can take advantage of cylindrical symmetry and rewrite the wave equation as follows:

$$\frac{1}{r} \frac{\partial}{\partial r} \left(r \frac{\partial W}{\partial r} \right) + \frac{1}{r^2} \frac{\partial^2 W}{\partial \theta^2} + \frac{\partial^2 W}{\partial z^2} - \left(\frac{n}{c} \right)^2 \frac{\partial^2 W}{\partial t^2} = 0 \quad (3.4)$$

By making a Fourier integral expansion in ω before combining equations in 3.1, one can write the

Helmholtz wave equation:

$$\nabla^2 W + \mu\epsilon \frac{\omega^2}{c^2} W = 0 \quad (3.5)$$

Now we can rewrite Helmholtz equation in the cylindrical coordinate system

$$\frac{1}{r} \frac{\partial}{\partial r} \left(r \frac{\partial W}{\partial r} \right) + \frac{1}{r^2} \frac{\partial^2 W}{\partial \theta^2} + \frac{\partial^2 W}{\partial z^2} + K^2 W = 0 \quad (3.6)$$

where $\left(\frac{n\omega}{c} \right)^2$ constant is substituted by K^2 as the wave vector.

Using separation of variables technique, we can solve this equation for each variable.

Considering the symmetry, one can simply acquire the following solutions:

$$W(z) = \exp(-jK_z z) \quad (3.7)$$

$$W(\theta) = \exp(\pm jm\theta) \quad (3.8)$$

$W_r(r)$ is solved by Bessel's equation of order m

$$\frac{d^2 W_r}{dr^2} + \frac{1}{r} \frac{dW_r}{dr} + \left(K^2 - K_z^2 - \frac{m^2}{r^2} \right) W_r = 0 \quad (3.9)$$

Let's substitute $\mathfrak{K}_n^2 = K_n^2 - K_z^2$; ($n=1,2,3$). Due to the azimuthal symmetry, one can set

$m=0$. The solution to $W_r(r)$ can then be written in terms of Bessel functions, i.e.

$J_0(\mathfrak{K}_n r), K_0(\mathfrak{K}_n r)$. For the inner layer, one should consider $J_0(\mathfrak{K}_1 r)$ only since

$Y_0(\mathfrak{K}_1 r)$ has a singularity at $r=0$. The outer layer can take a linear combination of both

terms, $K_0(\mathfrak{K}_2 r)$ where $r_1 \leq r \leq r_2$ since there is no lateral propagation. Note that the

aspect ratio (radius vs. thickness) allows us to use this approximation. In fact, using

$K_0(\mathfrak{R}_2 r)$ guarantees normalization of the wave intensity. Note that Hankel functions^{xxvii} cannot be used since their asymptotic behavior represents propagating plane wave,^{xxvii} that is

$$\lim_{r \rightarrow \infty} H_0^{(1)}(\mathfrak{R}r) \cdot e^{-j\alpha r} = e^{j(\mathfrak{R}r - \alpha r)} \quad (3.10)$$

Applying boundary conditions at the interface $r = r_1$ requires the following:

$$W_r(\mathfrak{R}_1 r) = W_r(\mathfrak{R}_2 r) \quad \text{at} \quad r = r_1 \quad (3.11)$$

We can rewrite these sets of equations in the following form:

$$c_1 J_0(\mathfrak{R}r) \Big|_{r=0} = 1 \Rightarrow c_1 = 1 \quad (3.12)$$

$$\begin{cases} c_1 J_0(\mathfrak{R}_1 r) = c_2 K_0(\mathfrak{R}_2 r) \\ c_1 \mathfrak{R}_1 J_1(\mathfrak{R}_1 r) = c_2 \mathfrak{R}_2 K_1(\mathfrak{R}_2 r) \end{cases} \quad (3.13)$$

Note that

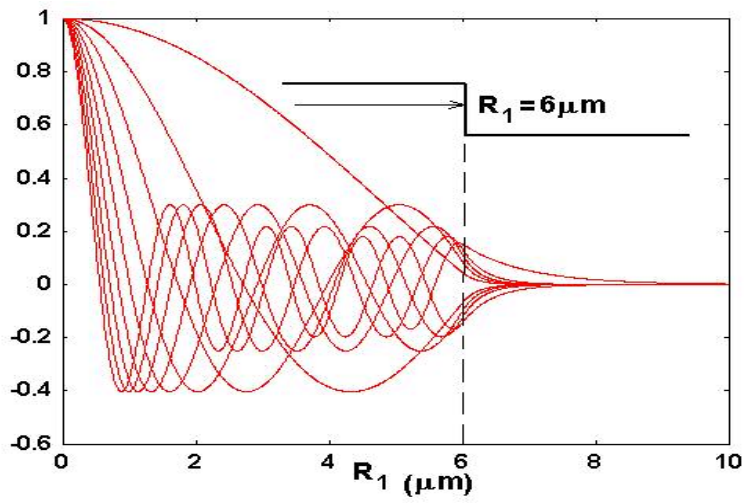
$$\frac{d}{dr} c_1 J_0(\mathfrak{R}_1 r) = -c_1 \mathfrak{R}_1 J_1(\mathfrak{R}_1 r) \quad (3.14)$$

$$\frac{d}{dr} c_2 K_0(\mathfrak{R}_2 r) = -c_2 \mathfrak{R}_2 K_1(\mathfrak{R}_2 r) \quad (3.15)$$

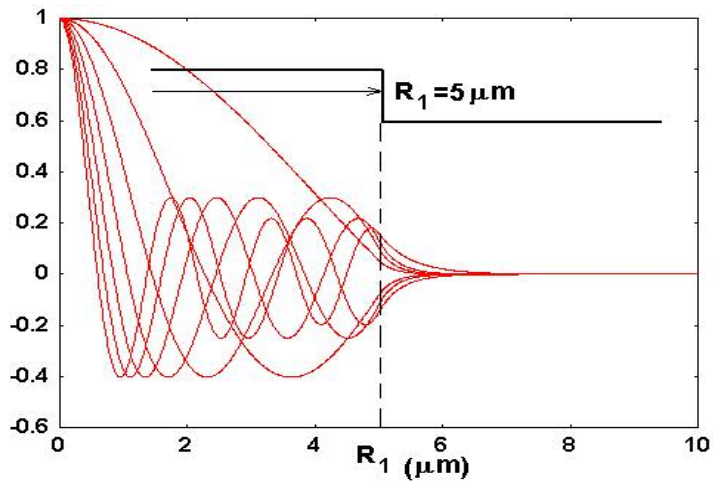
By solving equations (12) simultaneously one can provide the correct K_z which can ultimately be used to calculate VCSEL's lateral modes. Bisection method^{xxvii,xxvii,xxvii} was used to calculate the roots of these equations.

3.3 Simulation Results

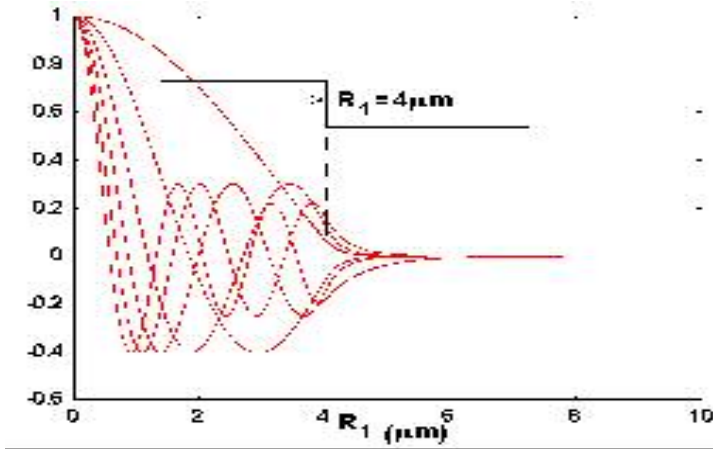
Fig. 3.1(a-d) shows the typical output of these equations. The dimensions and parameters of the VCSEL are given in the input file of the simulation. (Tab. 3.1)



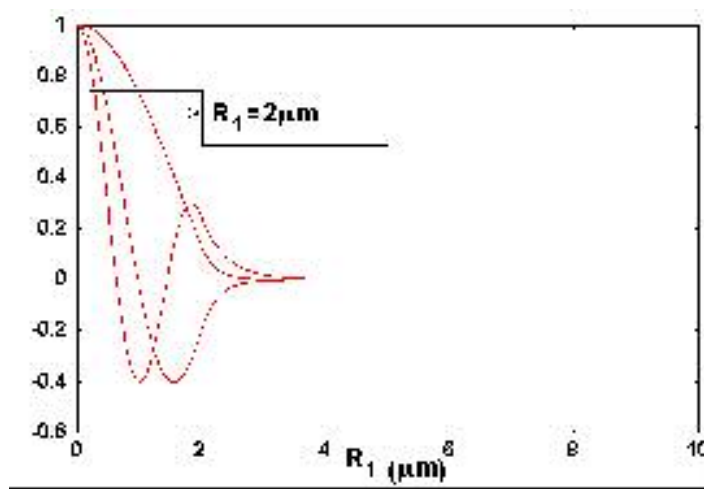
a)



b)



c)



d)
Fig. 3.1) VCSEL lateral modes for different pillar sizes, a) $R_1 = 6\mu m$, b) $R_1 = 5\mu m$, c) $R_1 = 4\mu m$, d) $R_1 = 2\mu m$

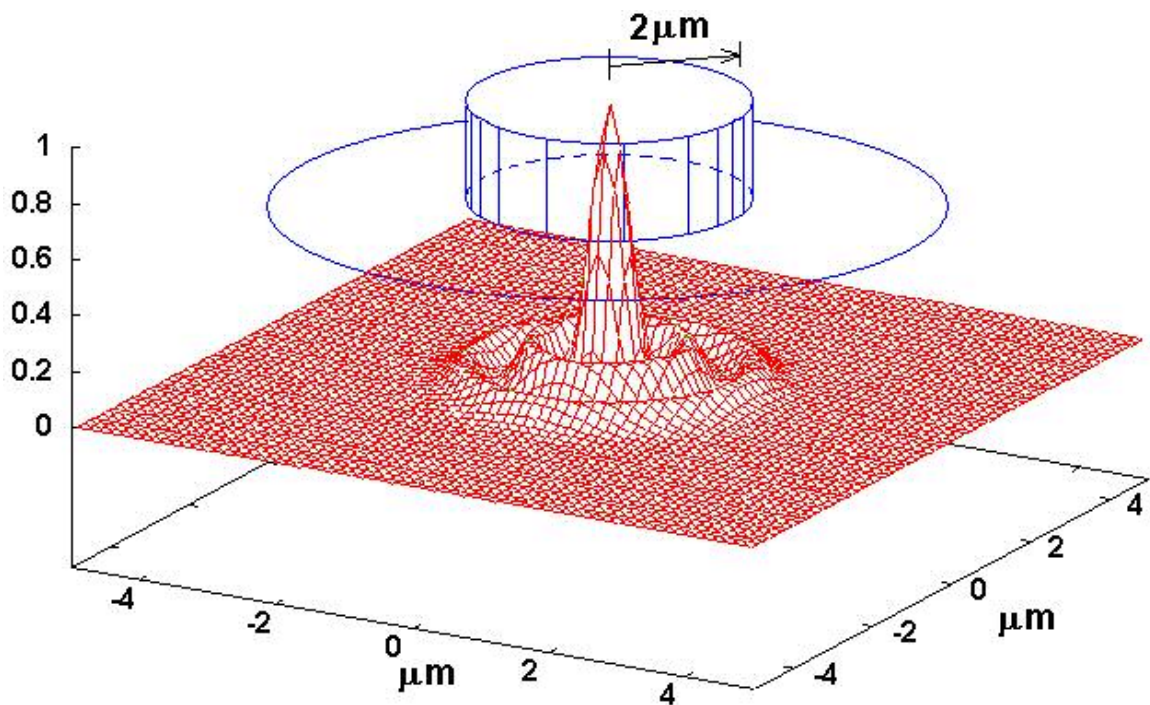


Fig. 3.2) 3D view of the lateral mode for $R_1 = 2\mu m$

```

!----- VCSEL PARAMETERS -----
4.7      1.46 ; Refractive Index n1, n2
4.0      ; Wavelength (in um)
2.  20.   ; Radius r1, r2 (in um)
!-----

```

Tab. 3.1) VCSEL input file in text format

This simulation can be used to optimize VCSEL pillar dimensions in order to reduce the lateral mode harmonics. This in turn lowers the pumping threshold and laser linewidth.

REFERENCES:

**CHAPTER 6: TE-COOLED OPTICALLY PUMPED MID-INFRARED
EXTERNAL CAVITY TUNABLE VCSEL**

6.1 Optical Cavity Resonators

Almost^{xxvii} all lasers require an optical cavity resonator. The main purpose of having a resonant optical cavity is to provide a sustainable stimulated photon generation by creating a positive feedback. Similar to any acoustic instrument (all musical instruments), an optical cavity resonator is designed to amplify a discrete set of allowed modes and to suppress otherwise. This in turn increases the wavelength selectivity and narrows the laser output spectrum (i.e. linewidth).

Now, let's try to review different types of cavity resonators. The simplest way to create a cavity resonator is to put two planar mirrors in parallel at a given distance say L . As shown in Fig. 6.1 this configuration induces a planar wave profile, traveling back and forth inside the cavity.

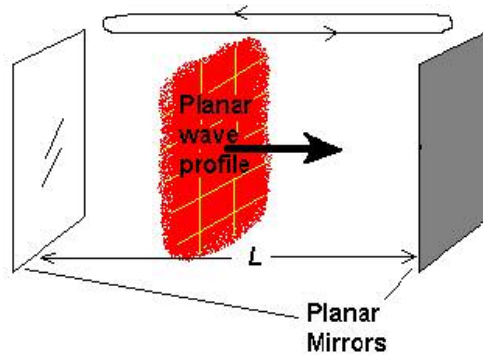


Fig. 6.1

Since there is no perfect mirror, for a round trip propagation of the wave one should expect some optical intensity losses and a phase shift. The former is due to the reflection efficiency of each mirror. To summarize the latter, we can introduce the round trip phase shift (RTPS), $2\theta = 2kd$ which is not necessarily an integral multiple of 2π . By introducing an angle ϕ , the deficiency can be written as

$$\phi = n(2\pi) - 2kL \tag{6.1}$$

where n is an integer. In order to have resonance, ϕ must be zero. Therefore

$$RTPS = 2kL = n(2\pi) \quad (6.2)$$

since $k = \omega \frac{n}{c} = \frac{2\pi}{\lambda}$, the resonant frequency can be written as

$$2L = n\lambda \quad (6.3)$$

Considering the possibility of error in alignment of the cavity mirrors, one can argue that the planar mirrors for the optical cavity are not a stable configuration. In fact, by looking at the stability diagram^{xxvii}, it is clear that planar mirrors' setup has a tendency to become unstable. However, using a concave mirror whose focal plane is positioned on a planar

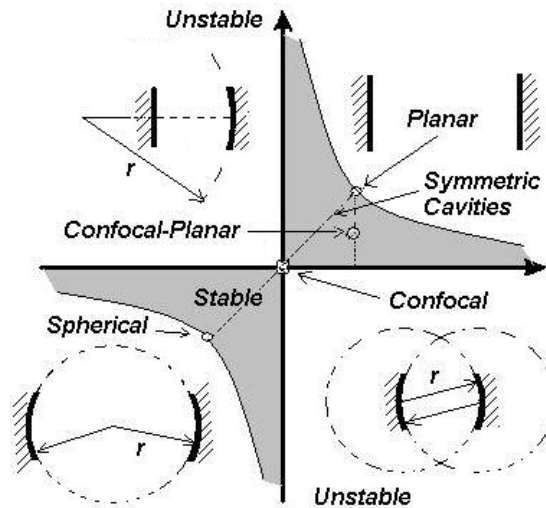


Fig. 6.2) Resonance cavity stability curve

mirror will provide a stable cavity that is tolerant to possible error in position and alignment (Fig. 6.2). It is important to note that the planar mirror width must be equal or smaller than the concave mirror width in order to have any tolerance to the misalignment. This configuration can also be constructed by introducing a convex lens into a planar mirror cavity (Fig. 6.3).

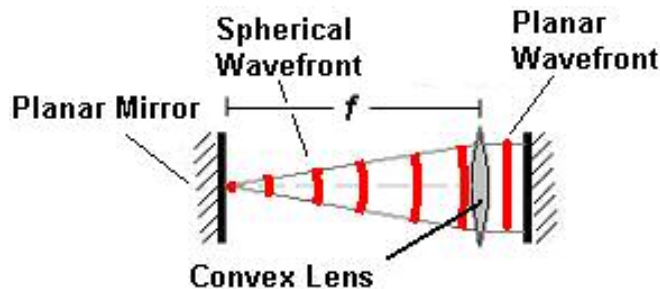


Fig. 6.3) Confocal-planar configuration using a planar cavity and a convex lens

Later on, we show how this configuration was used in our optical cavity resonator.

6.2 THE GRATING EQUATION

First, let's assume a simple case of monochromatic light. When the light reaches a grating surface (due to the periodic structure of the grating) it will be diffracted into discrete directions. Each grating groove can be considered as a very small, slit-like source of diffracted light. The overlapped (superposition principle) diffracted light form a diffracted wavefront^{xxvii}. The important fact of a grating is that a unique set of discrete angles exists in which, for a given spacing d between grooves, the diffracted light from all grooves are in phase, so they interfere constructively.

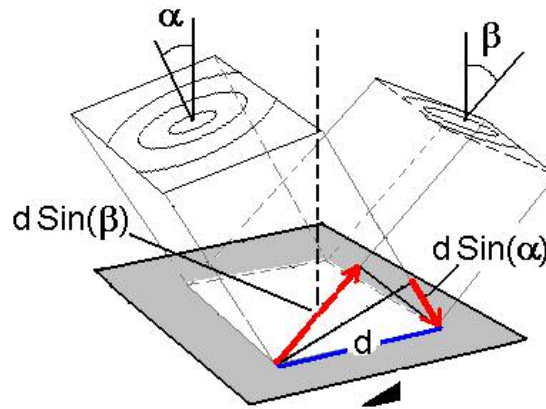


Fig. 6.4) The optical path difference of an incident and reflected wavefront caused by an optical grating

Figure 6.4 shows the geometry of diffraction by a reflection grating, where a light ray of wavelength λ incident at an angle α and diffracted along angle β by a grating with groove spacing d . These angles are measured from the grating normal, which is the dashed line perpendicular to the grating surface at its center. The sign convention for these angles depends on whether the light is diffracted on the same side or the opposite side of the grating as the incident light. For a reflection grating, the angles $\alpha > 0$ and $\beta_1 > 0$ (since they

are measured counterclockwise from the grating normal) while the angles $\beta < 0$ and $\beta_{-1} < 0$ (since they are measured clockwise from the grating normal. By convention, angles of incidence and diffraction are measured from the grating normal to the beam. This is shown by arrows in Fig 6.5.

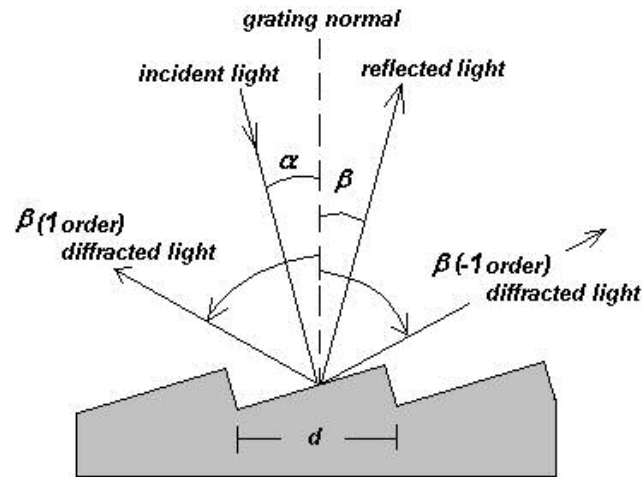


Fig. 6.5) Diffraction by a reflection grating

A beam of monochromatic light of wavelength λ is incident on a grating and diffracted along several discrete paths. The geometrical path difference between light from adjacent grooves is

$$\Delta = d[\sin(\alpha) + \sin(\beta)] \quad (6.4)$$

The principle of interference dictates that if this difference equals to some integral multiple of wavelength λ of the light, then the light from adjacent grooves be in phase (causing a constructive interference). For all other angles β , partial destructive interference occurs between the wavelets originating from the groove facets. This can be written as the grating equation which governs the angles of diffraction from a grating of

$$m\lambda = d[\sin(\alpha) + \sin(\beta)] \quad (6.5)$$

groove spacing d . Integer m is the diffraction order (or spectral order). For a particular wavelength λ , all values of m for which $2d > m\lambda$ correspond to physically observable diffraction orders. Since the number of grooves per unit length (i.e. mm^{-1}) is the standard way to identify a grating, it is convenient to write the grating equation as

$$Gm\lambda = \sin(\alpha) + \sin(\beta) \quad (6.6)$$

where $G = 1/d$ is the groove frequency or groove density. Eq. (6.5) and its equivalent Eq. (6.6) are the common forms of the grating equation. This is called in-plane diffraction (Fig. 6.6).

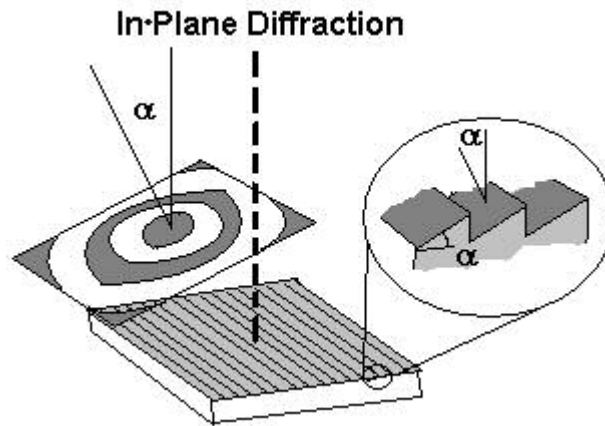


Fig. 6.6) In-plane diffraction from a diffraction grating with groove angle α

If the incident light beam is not perpendicular to the grooves, the grating equation needs to be modified. By introducing a new angle ϵ one can rewrite the grating equation as

$$Gm\lambda = \cos(\epsilon) (\sin(\alpha) + \sin(\beta)) \quad (6.7)$$

where ϵ is the angle between the incident light path and the plane perpendicular to the grooves at the grating center. If the incident light lies in this plane, $\epsilon = 0$. In geometries for which $\epsilon \neq 0$, the diffracted spectra lie on a cone rather than in a plane, so such cases are termed conical diffraction (Fig. 6.7). For a grating of groove spacing d , there is a

purely mathematical relationship between the wavelength and the angles of incidence and diffraction.

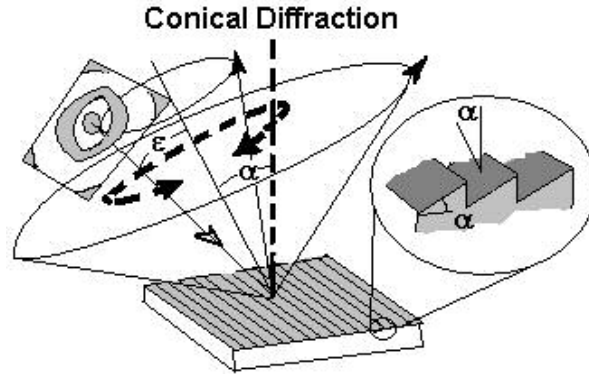


Fig. 6.7) Conical diffraction from a diffraction grating with groove angle α and beam angle ϵ

In a given spectral order m , the different wavelengths of polychromatic wavefronts incident at angle α are separated in angle:

$$\beta(\lambda) = \text{Sin}^{-1} \left(\frac{m\lambda}{d} - \text{Sin}(\alpha) \right) \quad (6.8)$$

When $m = 0$, the grating acts as a mirror, and the wavelengths are not separated ($\beta = -\alpha$ for all λ); this is called the zero order reflection.

An interesting case is when the light is diffracted back to its source (i.e., $\alpha = \beta$). This is called the Littrow configuration. The grating equation becomes

$$m\lambda = 2d\text{Sin}(\alpha) \quad (6.9)$$

In many applications (such as external cavity tunable lasers), the wavelength λ is changed by rotating the grating about the axis parallel with its central ruling, with fixed directions of incident and diffracted light. The deviation angle $2K$ (It is more convenient than K) between the incidence and diffraction directions is

$$\text{(angular deviation)} \quad 2K = \alpha - \beta = \text{Const.} \quad (6.10)$$

The scan angle ϕ is measured from the grating normal to the bisector^{xxvii} of the beams, whereas

$$2\phi = \alpha + \beta \quad (6.11)$$

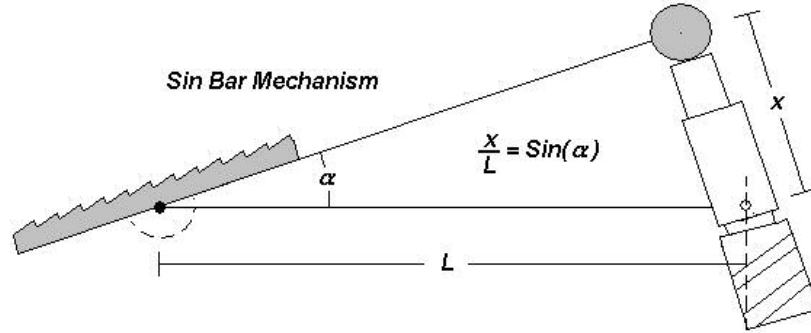


Fig. 6.8) A sine bar mechanism for wavelength scanning^{xxvii}.

As shown in Fig. 6.8, when the distance x extends or retracts linearly, the grating rotates by an angle ϕ where the $\sin\phi$ is proportional to x . Therefore, λ changes linearly with respect to x . Now let's rewrite Eq. 6.5 in terms of K and ϕ

$$\begin{cases} 2K = \alpha - \beta \\ 2\phi = \alpha + \beta \end{cases} \Rightarrow \begin{cases} \alpha = K + \phi \\ \beta = \phi - K \end{cases} \quad (6.12)$$

Therefore,

$$m\lambda = d(\sin(K + \phi) + \sin(\phi - K)) \quad (6.13)$$

$$m\lambda = d(\sin(K)\cos(\phi) + \sin(\phi)\cos(K) + \sin(\phi)\cos(K) - \sin(K)\cos(\phi))$$

$$m\lambda = d(\sin(\phi)\cos(K) + \sin(\phi)\cos(K)) \quad (6.14)$$

Thus, the grating equation can be expressed in terms of ϕ and the half deviation angle K as

$$m\lambda = 2d\cos(K)\sin(\phi) \quad (6.15)$$

For the Littrow configuration, Eq. 6.15 can be reduced to:

$$m\lambda = 2d\sin(\phi) \quad (\text{where } K=0) \quad (6.16)$$

substituting $\text{Sin}(\phi)$ by x/L as shown in Fig. 6.8,

$$m\lambda = 2d \frac{x}{L} \quad (6.17)$$

Eq. (6.17) shows that the diffracted wavelength by a grating in the Littrow configuration is directly proportional to the displacement x of the grating. This is the basis for external cavity wavelength tuning.

6.2.1 Resolving Power

The resolution or chromatic resolving power of a grating is defined as the ability to separate adjacent spectral lines. In general, resolution can be written as^{xxvii}

$$R = \frac{\lambda}{\Delta\lambda} \quad (6.18)$$

Theoretically, the resolution limit is

$$R = mN \quad (6.19)$$

where m is the diffraction order and N is the total number of grooves illuminated on the surface of grating. Using Eq. 6.5 one can substitute m in Eq. 6.19 and rewrite it as:

$$R = \frac{d(\text{Sin}(\alpha) + \text{Sin}(\beta))}{\lambda} N \quad (6.20)$$

where d is the width of a groove. Since $W = Nd$ is the width of the grating and $|\text{Sin}(\alpha) + \text{Sin}(\beta)| < 2$, then maximum attainable resolution can be written as:

$$R_{Max} = \frac{2W}{\lambda} \quad (6.21)$$

Assuming the grating parameters ($d=150$ 1/mm, $\text{Blaze}=17.5^\circ$, $W=50$ mm) used in the

experiment and at $\lambda_0 \approx 4\mu\text{m}$ Eq. 6.21 gives $R_{Max} \cong 25600$ or $\frac{R_{Max}}{\text{Wavenumber}} \cong 0.1\text{cm}^{-1}$

6.3 Ray-Tracing Simulation of Diffraction Grating Linewidth A Demonstration of Linewidth Spot-Size Dependency

One of the main limitations of diffraction grating performance in an external cavity configuration is poor lateral mode suppression when radiating spot size is relatively large.

To investigate this quantitatively, a simple model was devised.

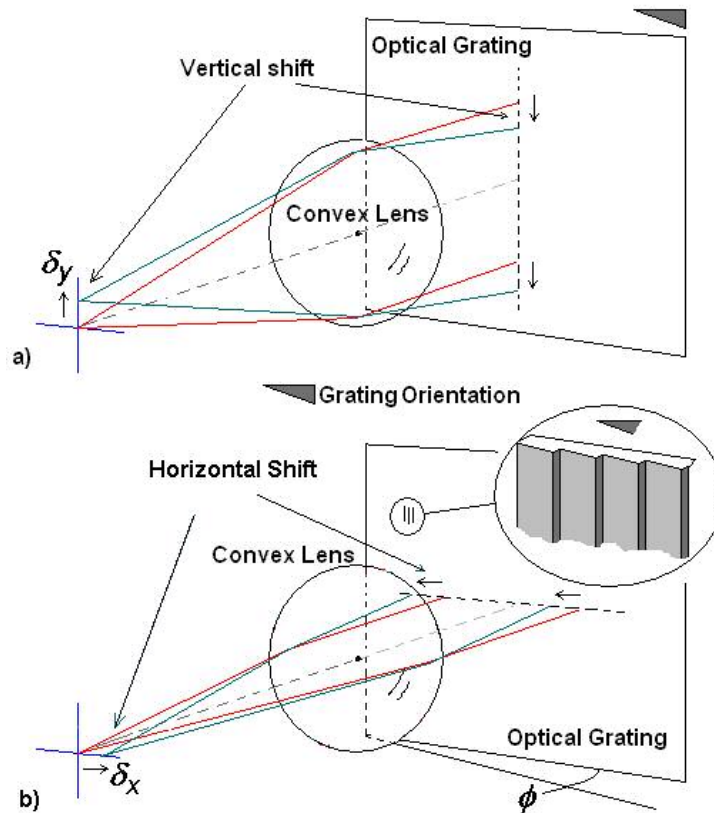


Fig. 6.9) Horizontal and vertical shift caused by source dislocation

As shown in Fig. 6.9, an upward vertical shift at the focal plane where the source is located will cause a downward vertical shift on the diffraction grating. Similarly, a right

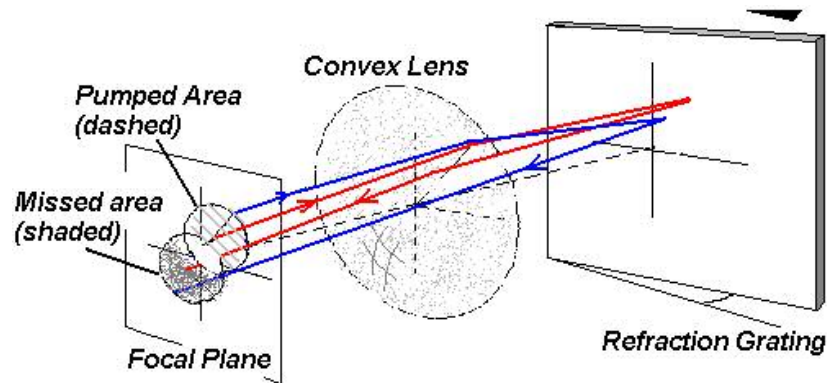


Fig. 6.10) An optical misalignment between the center of pump area (dashed area) and the optical axis will greatly increase optical loss. The missed area does not contribute to optical feedback of the cavity.

horizontal shift at the focal plane will make a left shift on the grating. It is important to note that since the grating groove-orientation is assumed to be parallel to the y-axis; vertical shift does not change the interference pattern from the grating. Therefore, the reflected beam will be unaffected by the shift. However, the desired retro-reflection property (when the diffracted beam returns to its source) of the axial beam is no longer valid. This vertical dislocation will not have a dramatic effect in laser performance, as long as the pumped area is centered to the optical axis (Fig. 6.10).

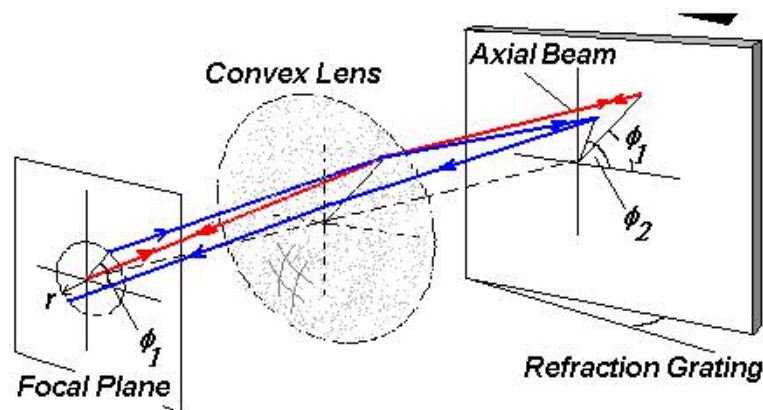


Fig. 6.11) Illustration of retro-reflection of an axial beam and a randomly positioned beam at (r, ϕ_1)

A horizontally shifted beam not only has a horizontal dislocation but also experiences diffraction with angular-dependency (Fig. 6.11).

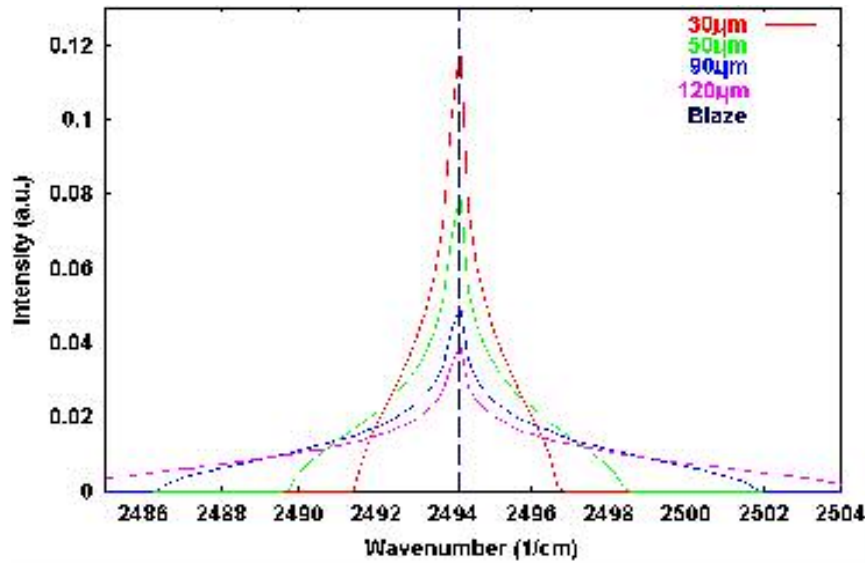


Fig. 6.12) Grating ($d=150$ 1/mm, Blaze= 17.5°) linewidth simulation result for different spot sizes

Assuming the thin-lens approximation and ignoring the near-field effect (focal length $\gg \lambda$), one can use the Monte-Carlo method to trace a large number of individual rays and do a segmented sum over wavelength for the returned beams^{xxvii}. By doing so, a profile emerges that shows how the spot size affects wavelength distribution of the cavity. (Fig. 6.12 and 6.13)

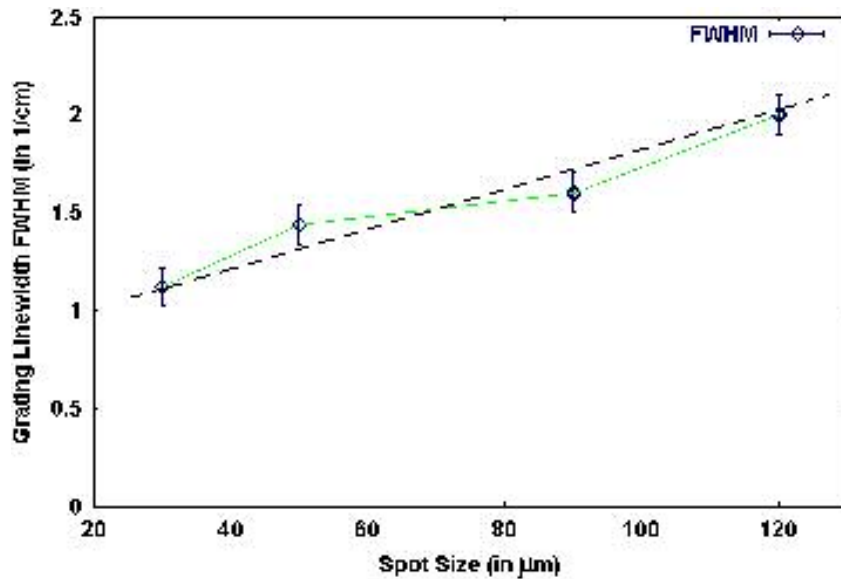


Fig. 6.13) Grating linewidth dependency on spot size (pumped area)

6.4 Tunable External Cavity Configurations

Adopted from spectroscopy, Littrow and Littman-Metcalf configurations^{xxvii-xxvii} are widely used for tunable laser systems^{xxvii-xxvii}. Both use an optical diffraction grating as a filter inside the cavity. In the Littrow configuration, the grating also plays another role as the end mirror of the cavity resonator,^{xxvii} which simplifies the configuration. As it was previously discussed, the Littrow configuration relies on the wavelength-selective retro-reflecting property of a diffraction grating when is positioned at its blaze angle as shown in Fig. 6.14.

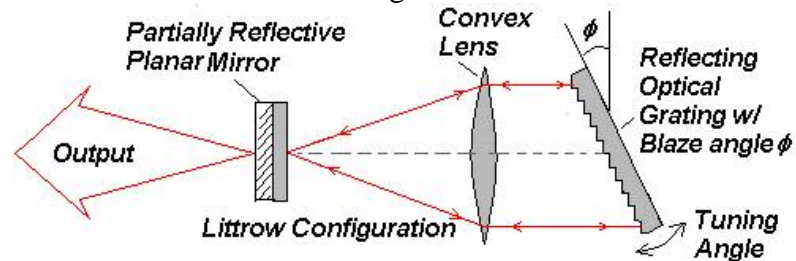


Fig. 6.14

It is important to mention that in the Littrow configuration, the cavity effective length is fixed. This causes mode-hop in the laser during the tuning process. The Littman-Metcalf configuration goes one step further by adding an extra mirror, which now is the end mirror of the cavity. When designed correctly, it allows tuning the laser emission wavelength and simultaneously corrects the effective cavity length (Fig. 6.15).

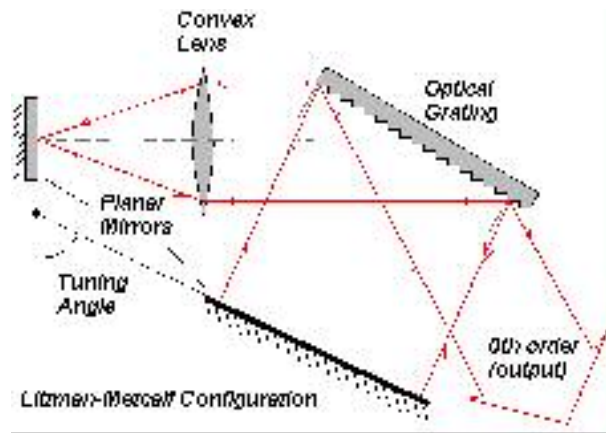


Fig. 6.15

However, this increases optical loss, which consequently reduces the output power. This is a crucial design factor when the laser output is low. Reviewing the pros and the cons of both methods suggests that the Littrow configuration is the simplest and most feasible approach toward an external cavity tunable mid-infrared laser.

6.5 A New Type of External Cavity Configuration

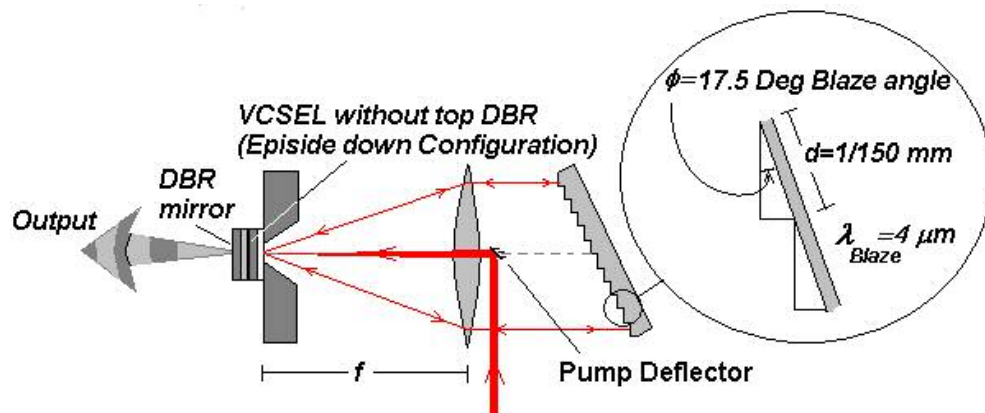


Fig. 6.16) Pseudo-axial optically pumped external cavity tunable laser configuration

Since optical pumping was the only available method at the time, a new form of external cavity was designed and built (Fig. 6.16). This design takes advantage of the existing convex lens in the cavity to focus the pump directly to the lasing spot on the substrate. A small deflector was positioned to redirect the pump and align it to optical axis of the cavity. This also allows easy positioning of the pump spot on the substrate. The convex lens acts as a magnifying glass and makes it very easy to observe (using an IR camera) the location of the pump spot on the substrate.

In the first prototype, tuning was done by a micrometer screw to change x and consequently change λ . There are other alternative methods that can be used to automate this process. One of the most accurate ways is to use piezoelectric actuators. A prototype driver was designed and built, but it was not integrated into the cavity. More details on the driver circuit are available in Chapter 7.

6.6 Experimental Results

The following graphs are the experimental data from this configuration.

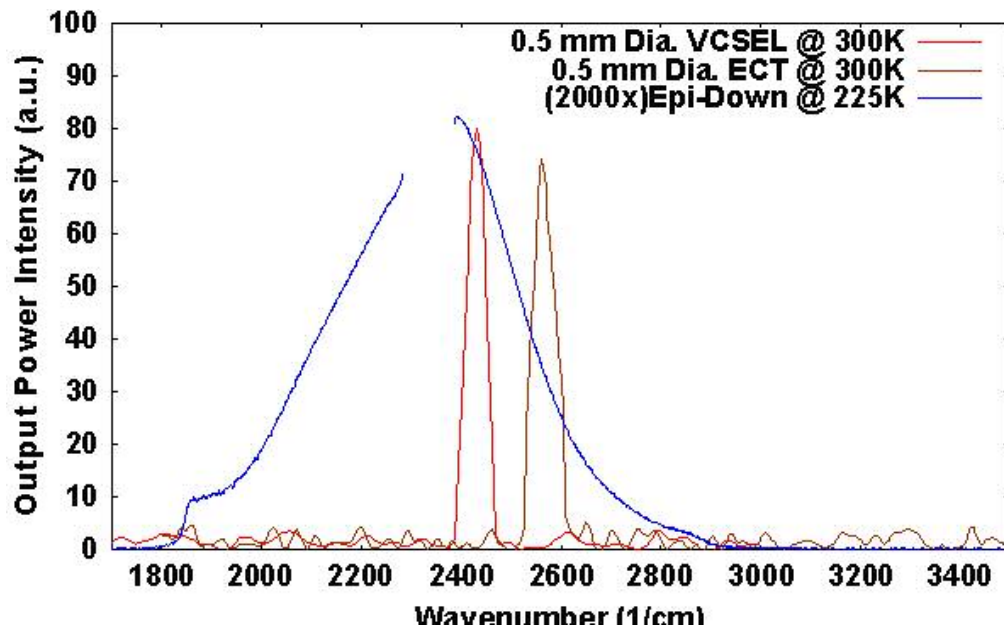


Fig. 6.17) ECT, VCSEL and photoluminescence linewidth comparison

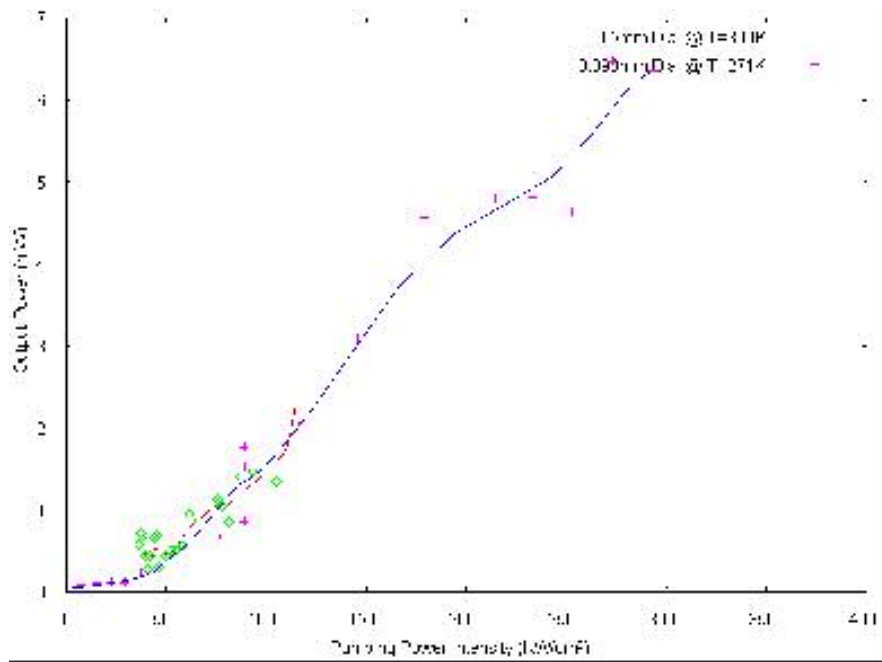


Fig. 6.19) P-P curve for ECT with 0.5mm And 90µm Dia. Spot size at 300 and 271K respectively

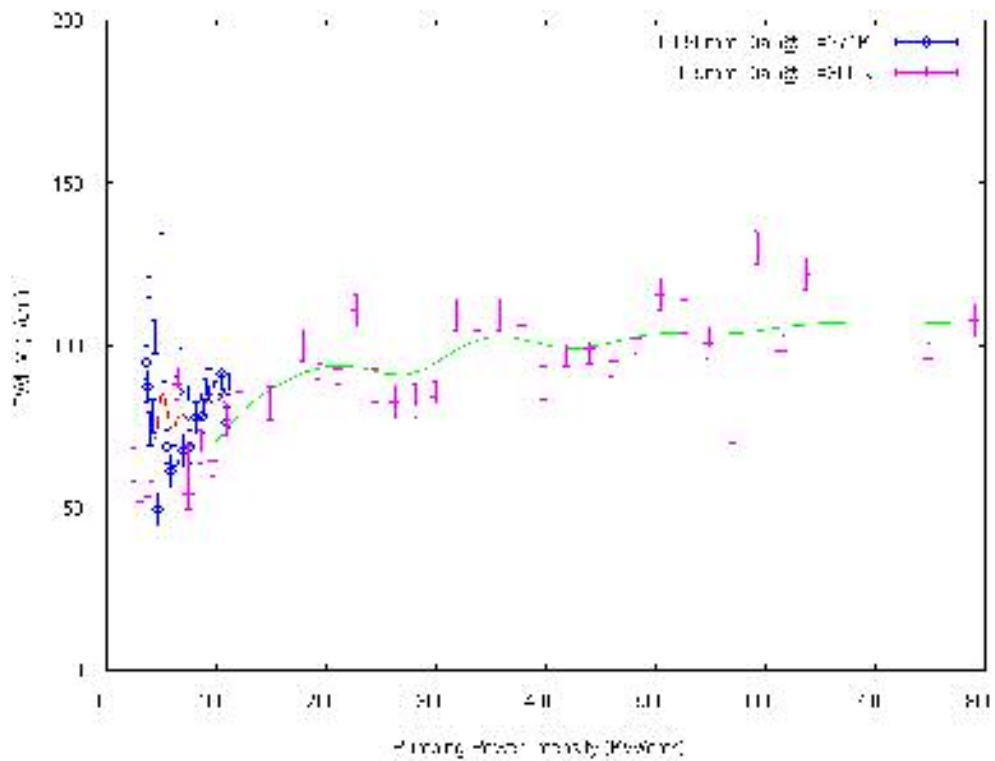


Fig. 6.20) Line width comparison of ECT at 271K and 300K

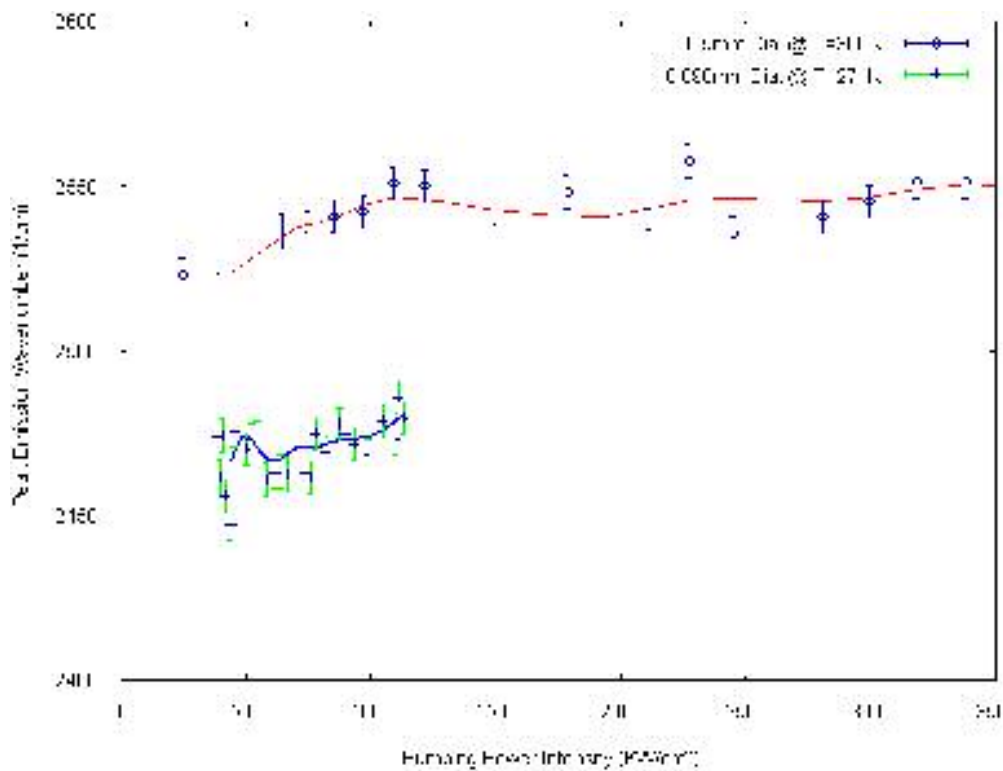


Fig. 6.21) Peak emission wavenumber comparison at 271K and 300K

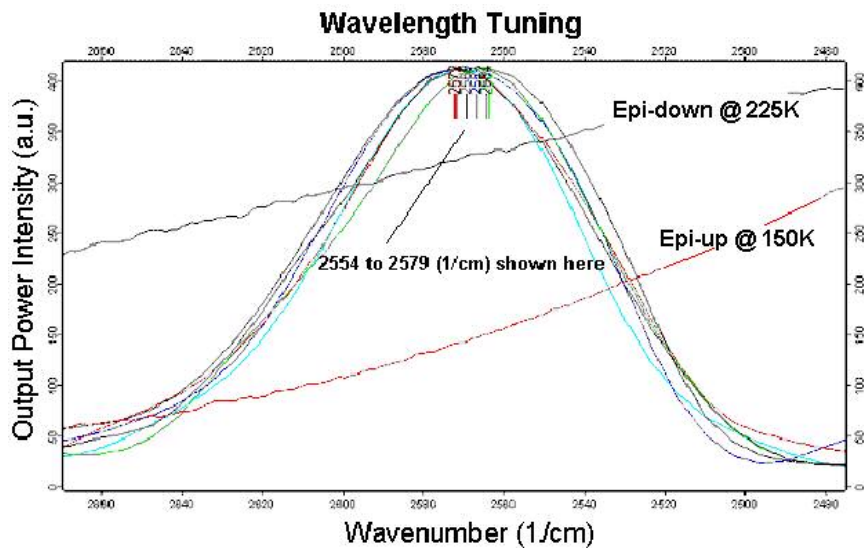


Fig. 6.22) Zoom-in plot of laser emission at different wavelengths in comparison with photoluminescence curves from epi-side down and epi-side up of the same substrate

6.7 Analysis

Experimental results clearly show that external cavity tuning can provide wide tuning range with a relatively simple mechanism. Also using epi-side down configuration will

enhance the heat dissipation which is generally the main obstacle of a IV-VI room temperature laser. However, despite all the efforts in this design, the laser still suffers from being overheated. Possible reasons for this shortcoming are 2D-sheet heat dissipation, relatively large distance to heat-sink (Fig. 6.23) and low quantum efficiency ($\lambda_{pump}=1.064\mu m$ and $\lambda_{laser}=4.0\mu m$).

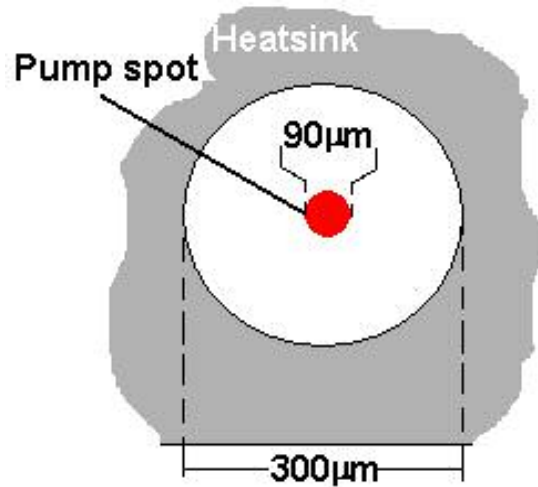


Fig. 6.23) (a) Pump spot and heat-sink rim size comparison

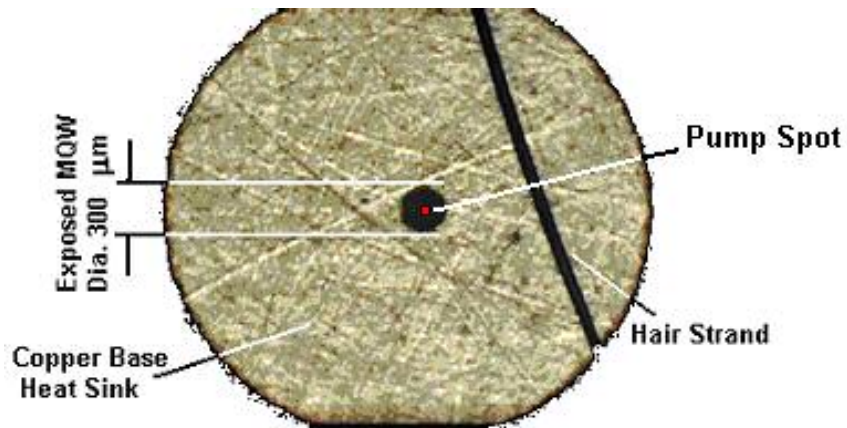


Fig. 6.23) (b) Front-view of exposed MQW and a hair strand as a scale reference

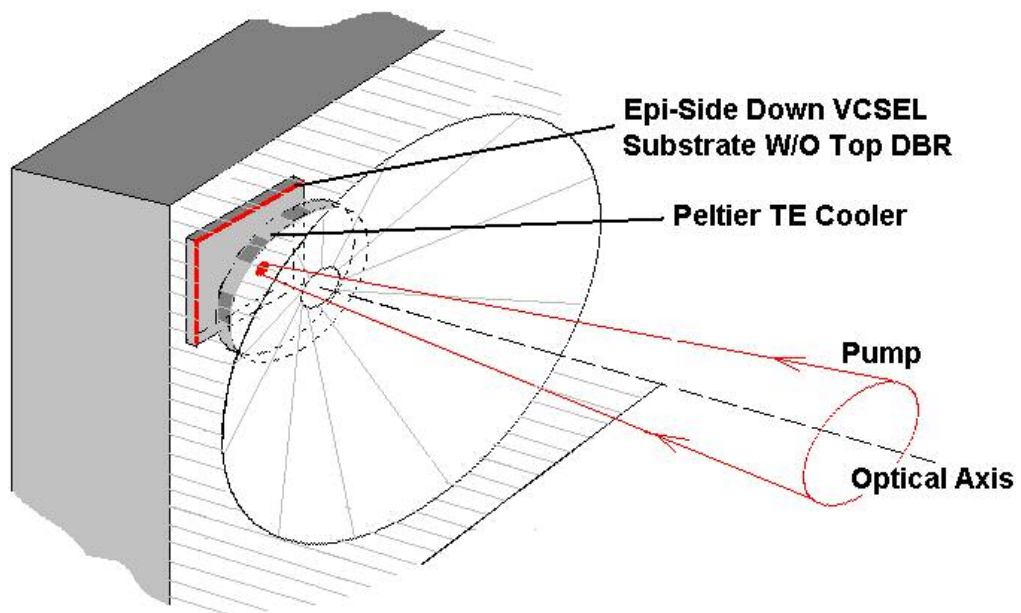


Fig. 6.24) An isometric view of ECT heat-sink base configuration

REFERENCES:

CHAPTER 7: INSTRUMENTATIONS AND UTILITIES

In this chapter, a brief description of several utilities including some optical/mechanical and electronic devices plus some software is presented. The main purpose of this chapter is to familiarize the reader with the tools that the author had to design and build in order to conduct this research.

7.1 OPTICAL DEVICES

7.1.1 Optical Steering Mechanism

Let's assume we want to direct a laser beam to a fixed surface (i.e. a sample) with a given incident angle. One trivial but cumbersome way is to move the laser and position it to the desired angle with respect to the sample orientation. On the other hand, by utilizing a very specific optical path which uses a minimum of three mirrors to create an axial symmetry as shown in Fig.1, one can change the incident angle without changing the laser's position.

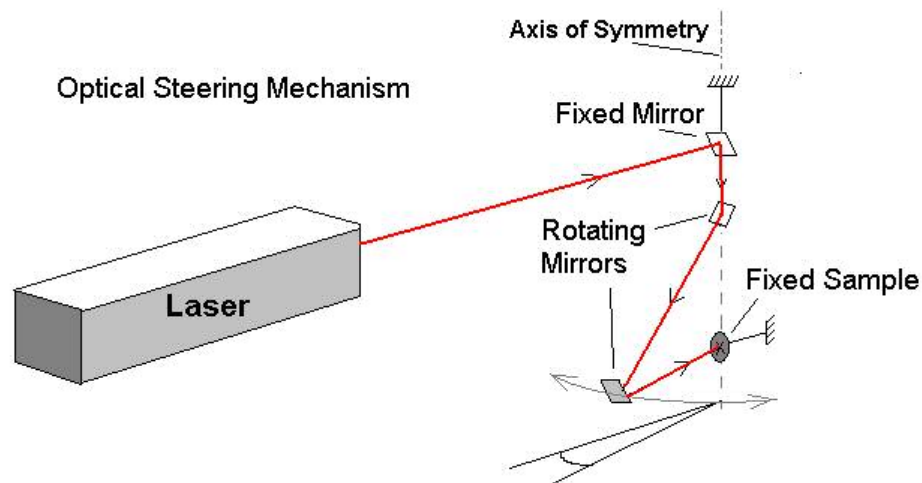


Fig. 7.1

This set up was used to measure the angular dependence of PL spectra and calibration of total PL power^{xxvii}. However, it is worthy to note that polarization angle will change by this mechanism, should it be a concern for a specific experiment.

7.1.2 Variable Angular Aperture

In order to study the angular distribution of emission from a VCSEL, a differential viewing angle is necessary. Since the VCSEL under investigation was an optically pumped laser, the author designed and built a device that utilizes a fixed V-groove and an adjustable cylindrical stop (Fig. 7.2).

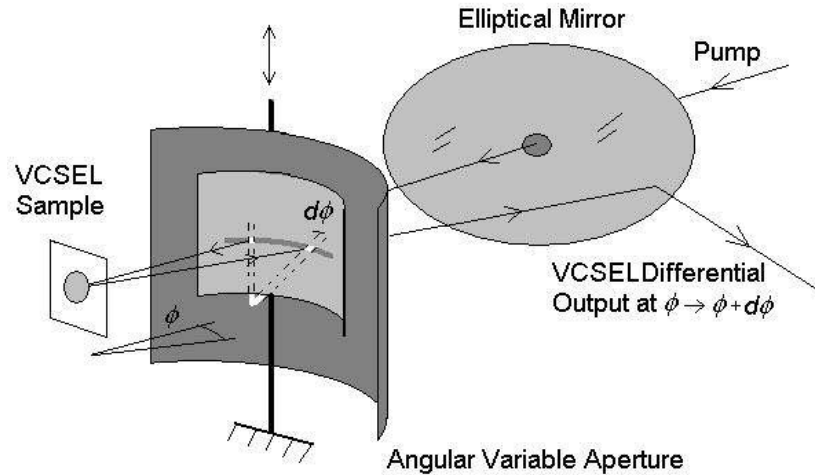


Fig. 7.2

This device allows the user to pump the sample directly at 90° while it can adjust the emission from the sample only at a specific differential angle.

7.1.3 Optical Position/Angle Sensor With Angle Magnifier Mechanism

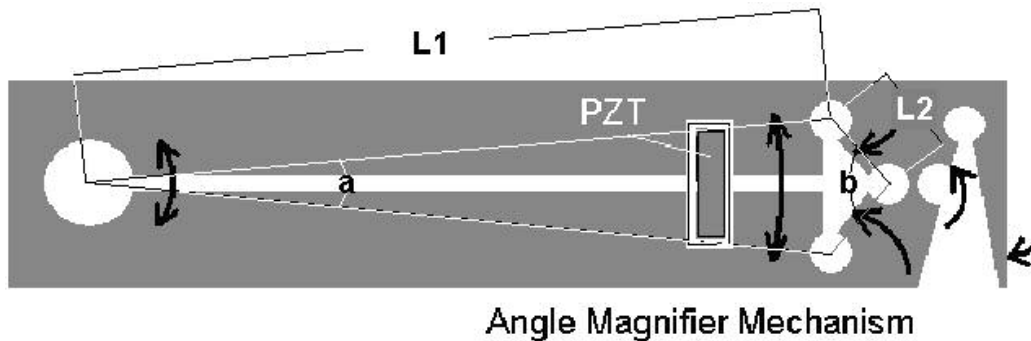


Fig. 7.3) Double Stage 10X Angle magnifier Mechanism with $L1/L2=5$

This device was designed to simplify angle detection of a PZT-driven optical grating stage. It basically uses a four-point diamond-shaped link mechanism.

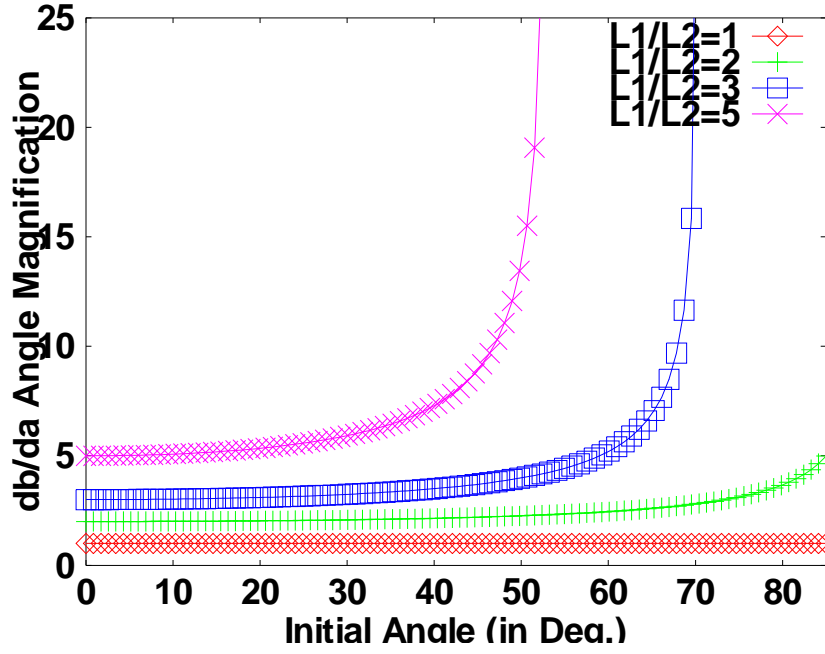


Fig. 7.4) Angle Magnification for four different L1/L2

In order to find the magnification rate, we start with the relations between the angles, a and b . The magnification can be written as

$$L_1 \sin\left(\frac{a}{2}\right) = L_2 \sin\left(\frac{b}{2}\right) \quad (7.1)$$

$$b = 2 \sin^{-1}\left(\frac{L_1}{L_2} \sin\left(\frac{a}{2}\right)\right) \quad (7.2)$$

$$\frac{db}{da} = \frac{\cos\left(\frac{a}{2}\right)}{\sqrt{\left(\frac{L_1}{L_2}\right)^2 - \sin^2\left(\frac{a}{2}\right)}} \quad (7.3)$$

Based on Eq. 7.3 the angle magnification can be plotted for different L_1/L_2 (Fig. 7.4). In order to sense the angle, one can either use optical or electrical methods. A proposed optical method consists of two polarizer filters, as shown in Fig. 7.5a. We also propose an electrical method, using a variable capacitor (Fig. 7.5b) attached to the end of a link mechanism. If the capacitor is integrated to a LC circuit, one can measure the angle by

monitoring the output frequency. This simplifies the measurement since there is no need for any A/D converter.

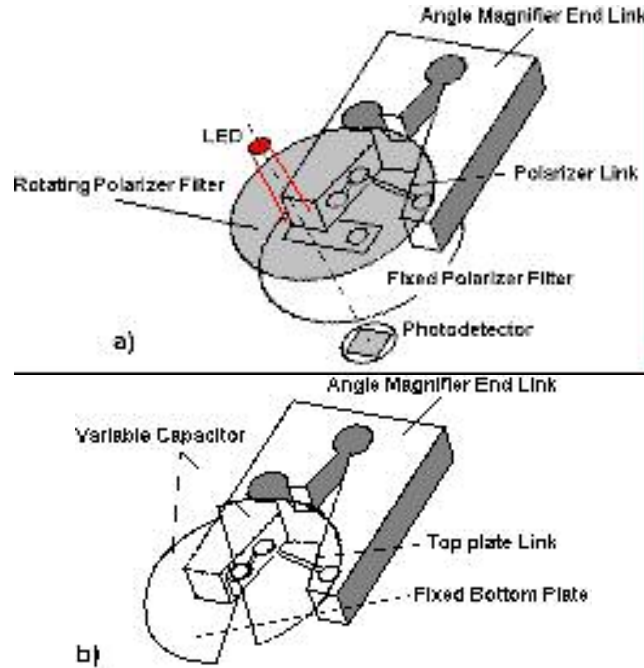


Fig. 7.5) Angle detection Mechanisms

7.1.4 Double B/S Pseudo-Axial Optically Pumped T-Configuration

This setup was designed for the measurement described in Chapter 4. Note that the pump deflector can be positioned in either location shown in Fig. 7.6.

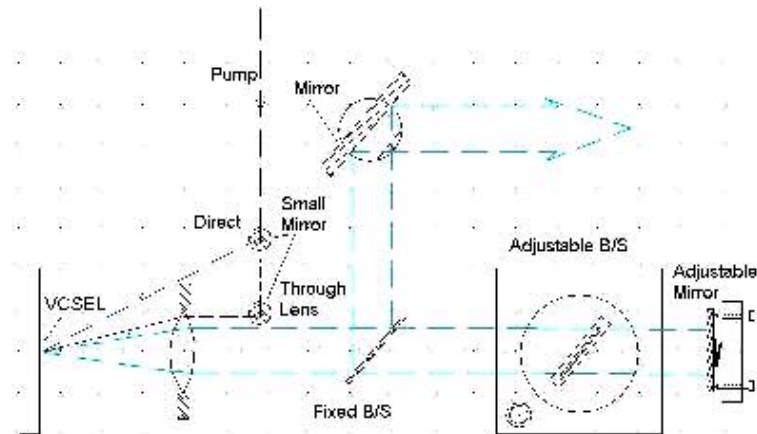


Fig. 7.6

7.1.5 Far-Field Direct Measurement Apparatus

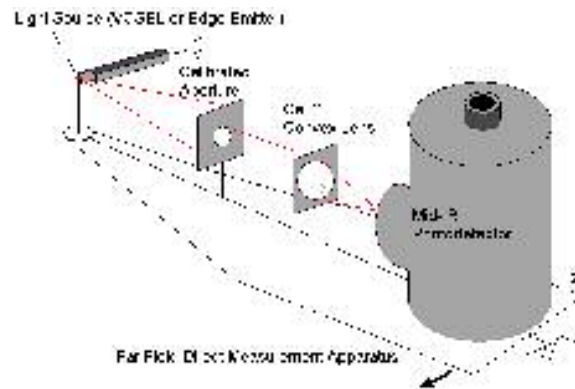


Fig. 7.7) Far-field measurement apparatus

Far-field measurement of a laser is an important issue. Such measurement provides useful information about the laser cavity and its overall performance. A simple stage with a fixed point was built (Fig. 7.7). By adding a calibrated aperture in front of a convex lens whose focal point is placed on the detector, an incremental measurement of light intensity becomes possible. For instance, a 5° aperture allows a minimum of 2.5° increment scan. For most practical purposes this is quite sufficient resolution to get a good far-field angular profile.

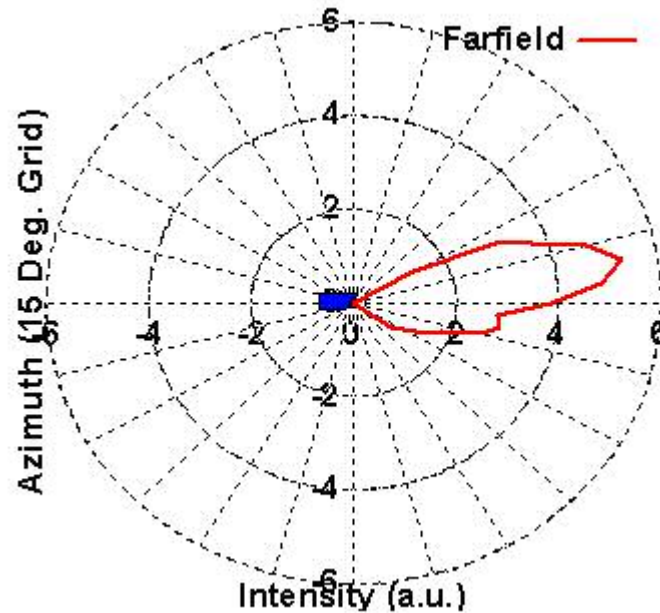


Fig. 7.8) Far-field pattern of an edge emitter mid-infrared source

Fig. 7.8 shows the experimental result for an edge emitting source. It is worthy to note that increase in the negative angle is caused by excessive radiation emitted from the top of the sample and not just from the facet itself.

7.1.6 Calibration of Nd-YAG duty Cycle by Measuring the Speed Of Light

It is clear that the accuracy of all measurements in this research depends on how accurately one can estimate the pumping power intensity. In order to verify the values from the laser (Nd-YAG) manufacturer, a fast recovery IR photo diode was used to measure the pulse width of the Nd-YAG laser. Surprisingly, the measurement showed the pulse width of 25-30nsec instead of the 5nsec claimed by the manufacturer. Later on, 5nsec pulse width was achieved at the maximum laser intensity. However the maximum laser intensity is too high for any practical purposes. This indeed had a significant effect on all of our measurements since it lowered the threshold pumping intensity by a factor of 6.

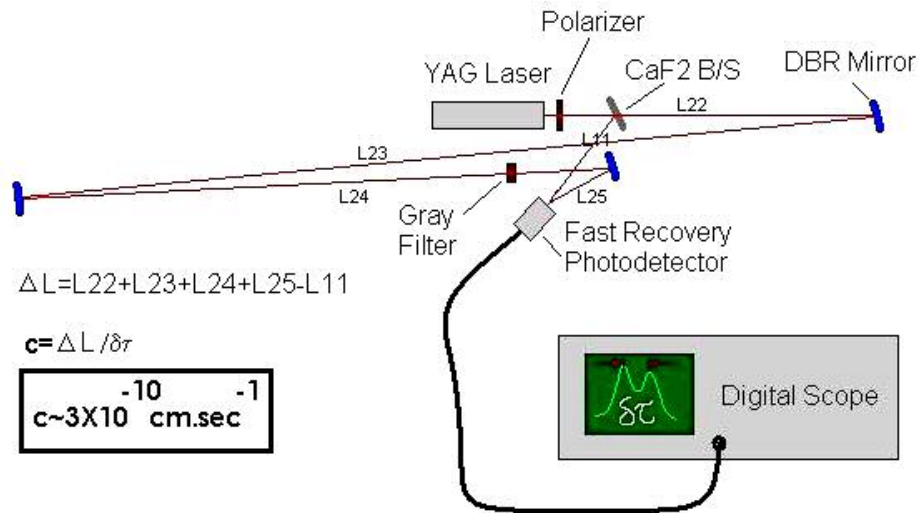


Fig. 7.9 (a) Schematic diagram of the speed of light measurement setup

In order to be absolutely sure about the new findings, a very reliable test was conducted to verify the timing accuracy of the experiment. As we all know, the speed of light is constant in all inertial reference frames. Therefore if we conduct a simple time of flight experiment with a laser pulse, we should be able to verify the timing accuracy of our system by measuring the speed of light for a known distance. The experiment consists of the Nd-YAG laser, a beam splitter and three DBR mirrors (Fig. 7.9 a, b).



Fig. 7.9 (b) Two-peak signal observed from the experiment.
 (Due to more reflection losses the second (shown on the right) peak is weaker.)

The experiment result confirmed that the oscilloscope timing is correct.

7.1.7 Pseudo-Axial Optically Pumped Tunable External-Cavity Apparatus

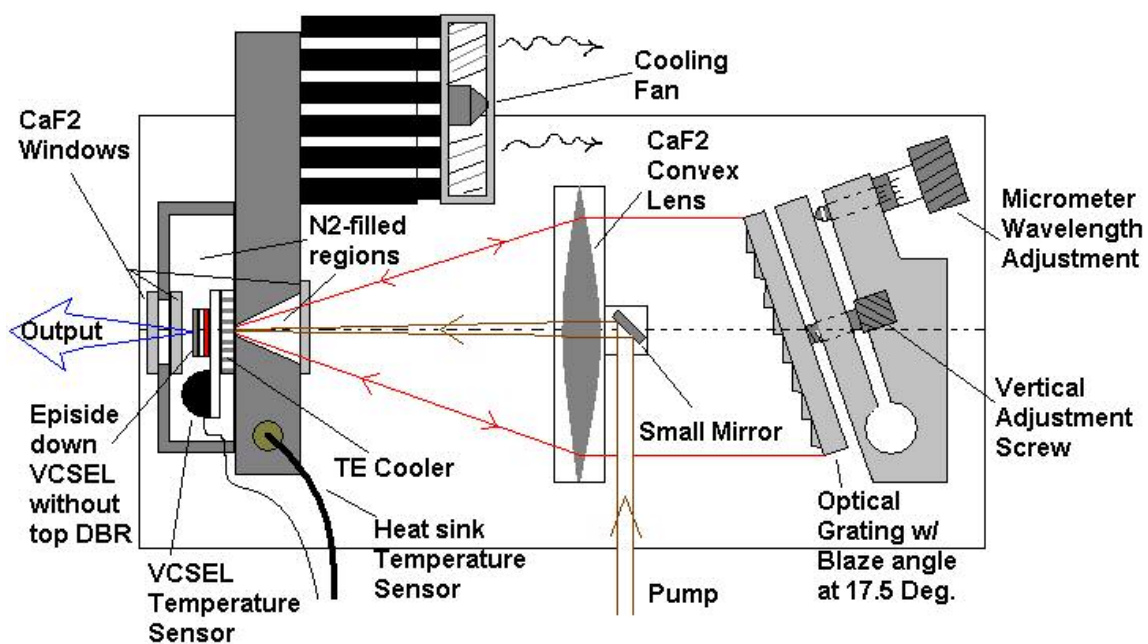


Fig. 7.10 (a) Schematic diagram of ECT

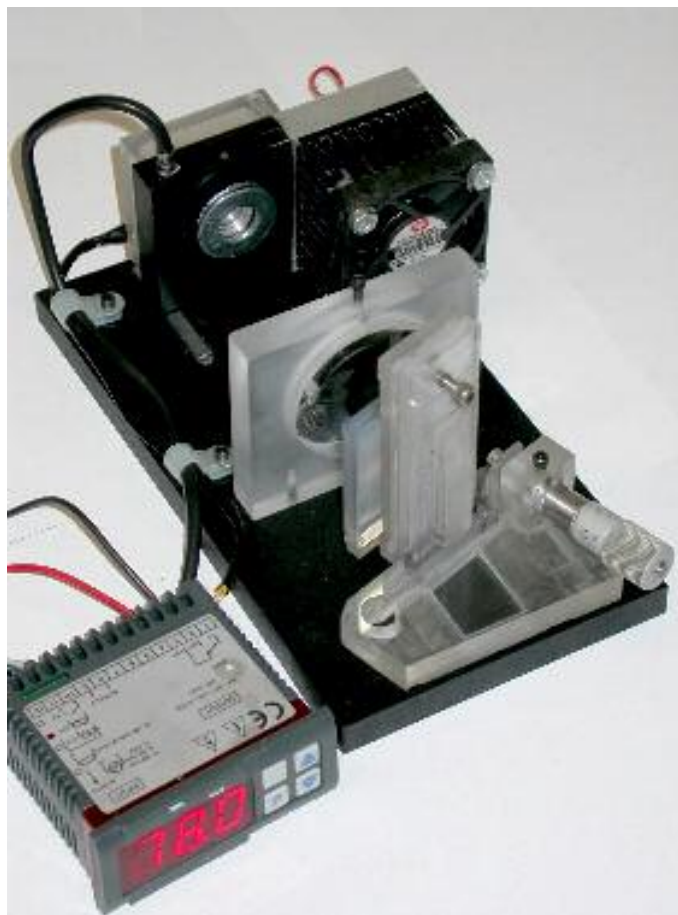


Fig. 7.10 (b) Rear-view of ECT described in chapter 6

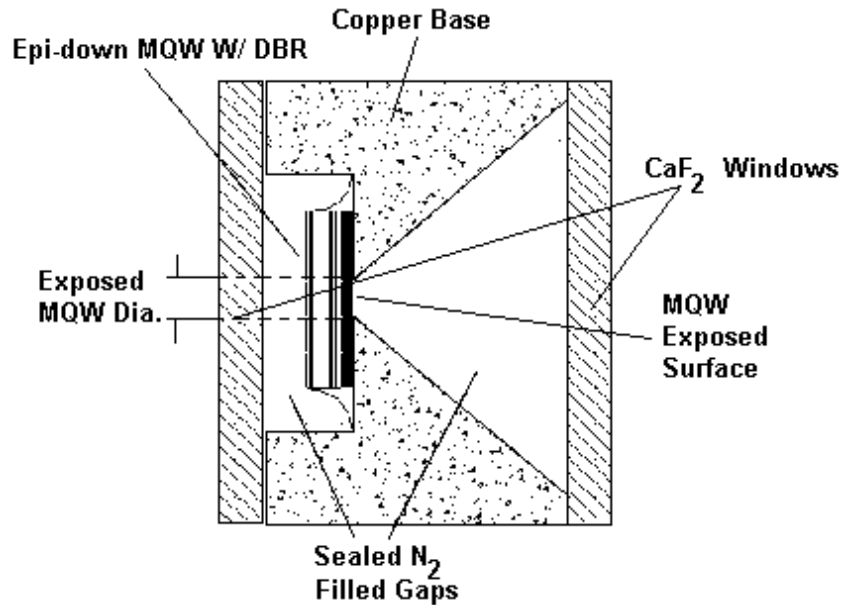


Fig. 7.11) Sealed Nitrogen-filled MQW encapsulation

During the experiment with TE-cooled system at subfreezing temperatures (271-273K) it became clear that moisture precipitation on the laser surface can seriously obscure the optical path and dramatically reduce its output power. To prevent that, simple nitrogen filled encapsulation was devised (Fig. 7.11). Since nitrogen has no absorption in the laser operating wavelengths, there will not be any change in the laser output spectrum. However in a more sophisticated system vacuum would be preferred.

7.2 ELECTRONIC DEVICES

7.2.1 PWM Controlled Peltier Driver

Peltier TE cool/heat device is a very simple and reliable temperature control system. Around certain operating current range, the Peltier device will perform very efficiently.

In most cases this range is from 1-5A. A driver is proposed to set and hold the temperature in the allowed operating range of the device. In most cases, the maximum gradient temperature is about 60C.

The concept of this design is a bi-directional voltage controlled pulse width modulation (PWM) astable oscillator. An N-typed MOSFET H-bridge power drive is the final stage of this system.

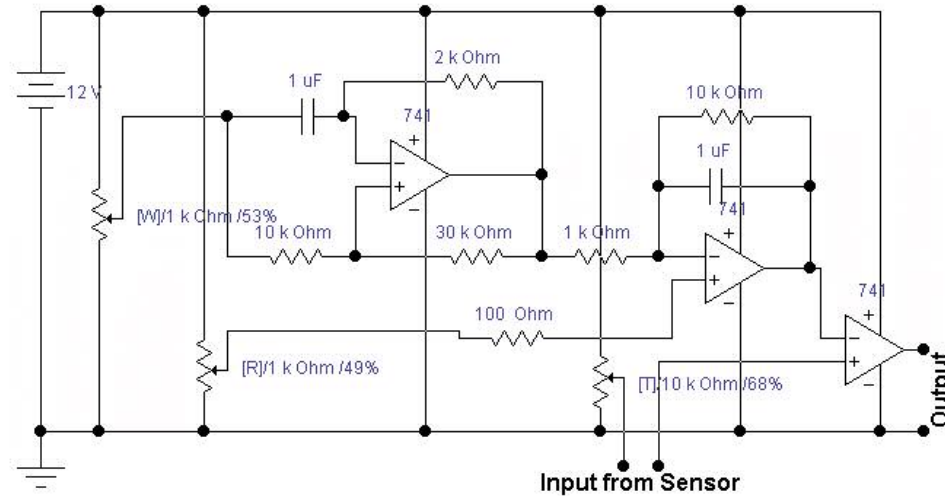


Fig. 7.13) Schematic Diagram of a typical PWM

The circuit consists of four separate stages. Stage 1 produces the clock at 1KHz. Stage 2 is an integrator, which converts squared clock train to symmetric triangular pulse train. Stage 3 is configured as a voltage comparator. In this stage the pulse train is compared to the reference voltage, provided by stage 4. The voltage of stage 4 is linearly proportional to temperature reading from IC temperature sensor. LM35 is a linear temperature sensor whose output changes by $10\text{mV}/\text{C}$ in its allowed operating range. The advantages of this design to direct current control are linearity and high efficiency. The final stage is simply an N-type MOSFET H-bridge configuration, which plays as a high current bi-directional power drive.

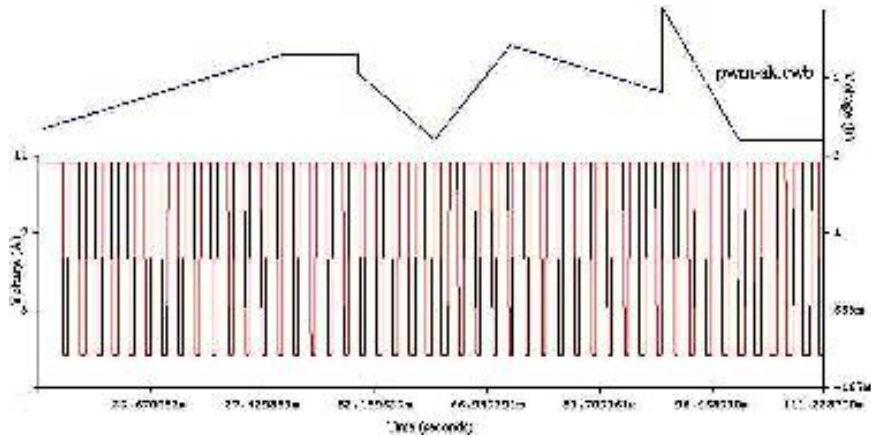


Fig. 7.14) PWM output for an arbitrary input waveform. Duty-cycle is proportional to the input.

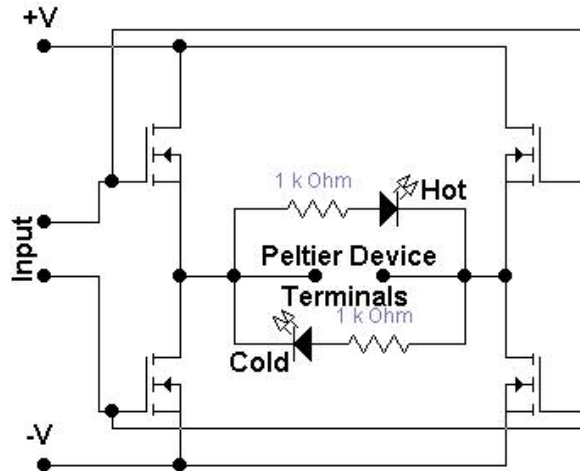


Fig. 7.15) MOSFET H-Bridge Driver for Peltier Cool/Heat System

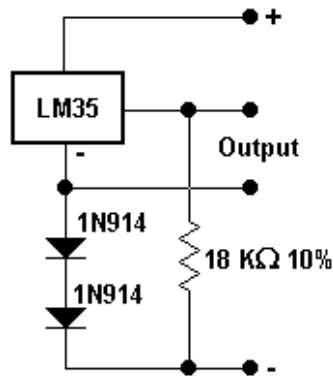


Fig. 7.16) LM35 Temperature sensor w/ extended range configuration^{xxvii}

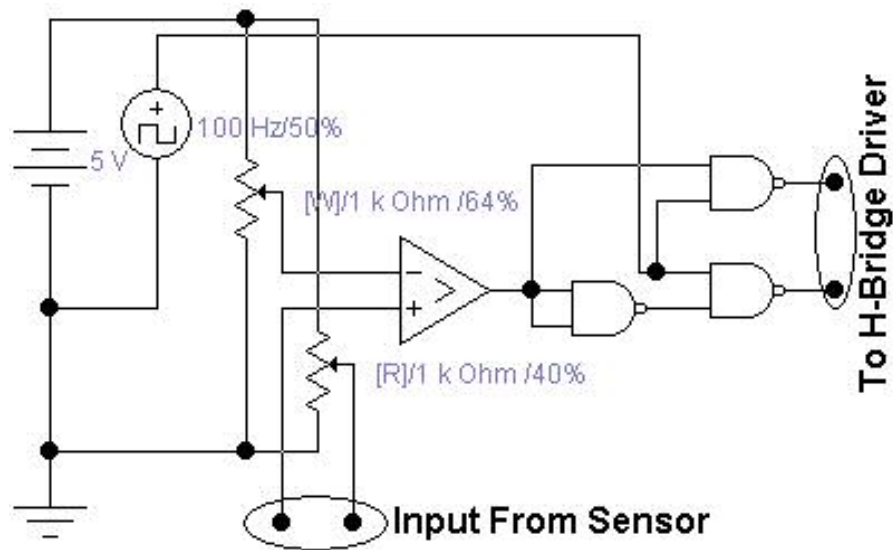


Fig. 7.17) A Bidirectional Driver for Cool/Heat System

7.2.2 PZT Micro-position Driver

An automated tunable external cavity requires an actuator. The actuator plays the same role as the micrometer screw described in section 7.1.7. Due to small displacement required for tuning, piezoelectric transducer/actuator is the most popular choice. Electrically PZT is a capacitor. The displacement of PZT ($L_{disp} \propto V_{PZT}$) is proportional to its voltage. If we assume this relation is linear, all one needs is a constant current source to actuate PZT linearly. Thus $L_{disp} = AV_{PZT}$ where A is a constant.

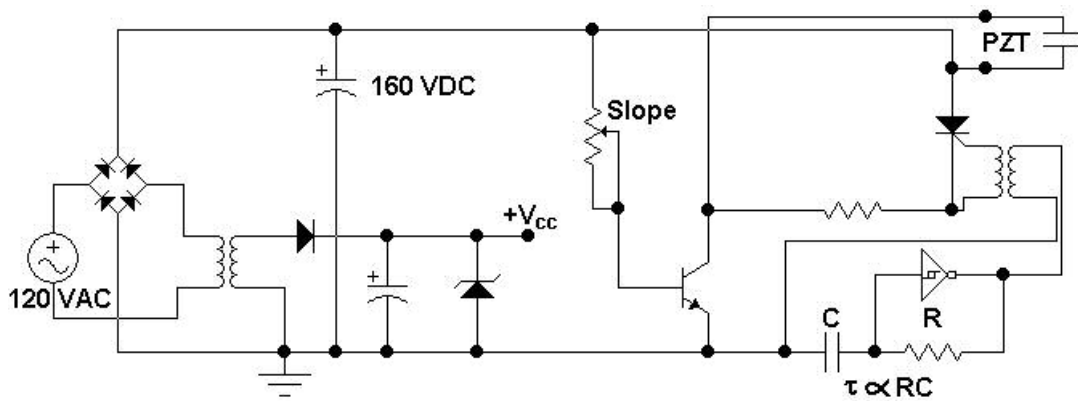


Fig. 7.18) Schematic diagram of PZT driver

$$\frac{dL_{disp}}{dt} = \frac{d}{dt} \left(\frac{Aq}{C} \right) = \frac{A}{C} \frac{dq}{dt} = \frac{A}{C} I \quad (7.4)$$

The proposed circuit shown in Fig. 7.18 consists of three sections. Starting from the left is a rectifying circuit which provides a high voltage DC around 160V and a low voltage DC for the oscillator. The second section is a high voltage PNP bipolar transistor which provides an adjustable constant current for PZT. The last section is a thyristor circuit which acts as a discharging switch. The oscillator is a simple RC Schmitt-trigger NOT gate. When adjusted correctly, the voltage across PZT will change with a saw-tooth pattern. (Fig. 7.19)

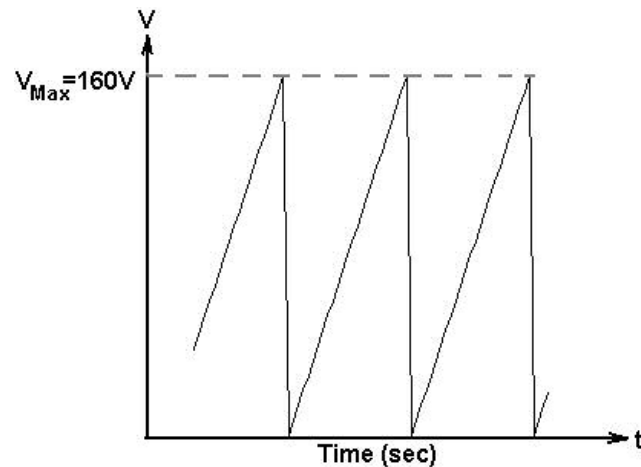


Fig. 7.19) Output waveform of PZT driver

7.3 UTILITY SOFTWARE PACKAGES

Throughout this research several pieces of utility software were developed. In this section, a brief discussion of each package is presented.

7.3.1 Laser Line-width Dependency of Optical Absorption Spectrum

This program can simulate the output spectrum of laser absorption spectroscopy for a given laser linewidth. This allows the user to estimate the minimum linewidth required to observe specific features of a sample spectra. For example if the true spectrum of a

sample is the top curve in Fig. 7.20(a-d), then the observed spectrum scanned by a laser with the linewidth shown at the center of each graph will be the bottom curve as shown in the figure.

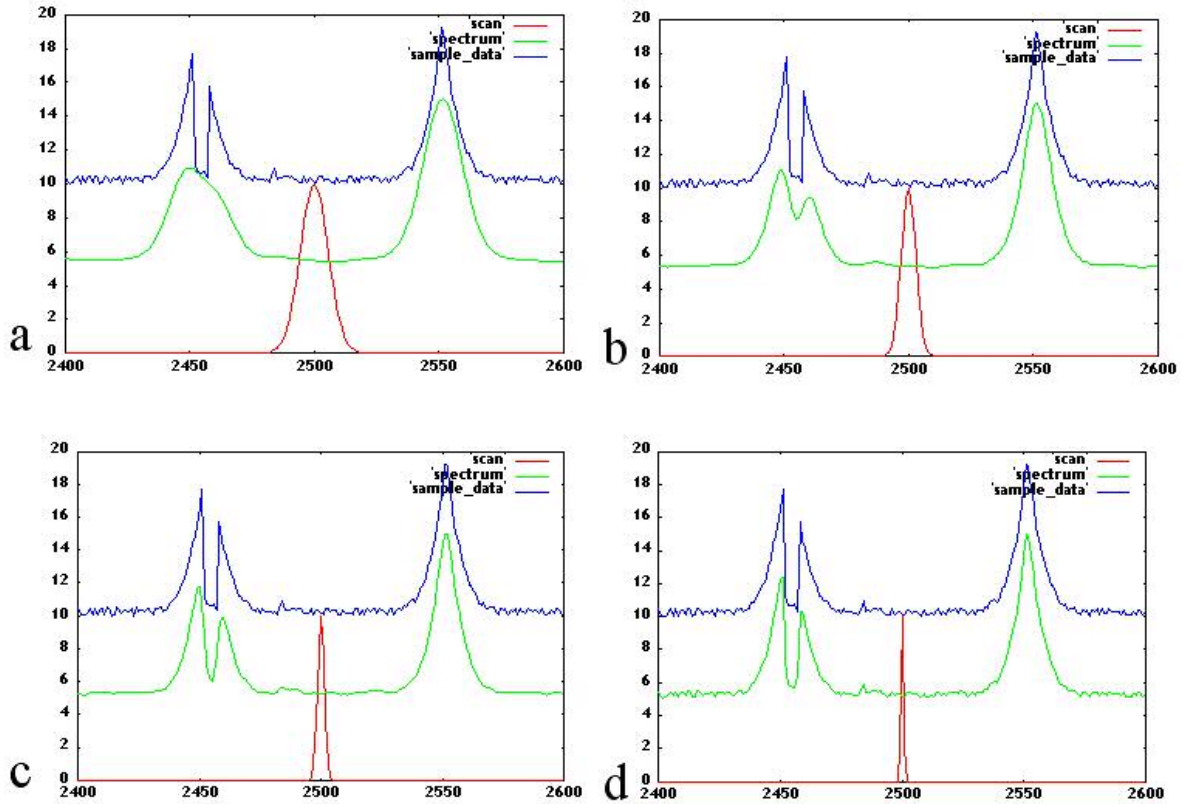


Fig. 7.20) Simulated output spectrum scanned by a tunable laser. The central peak shows the scanning laser linewidth.

7.3.2 Far-field Optical Profile Simulation Using Monte-Carlo Method

If the crystal orientation does not allow cleavage of laser facets, etching can be used instead. However isotropic behavior of wet etching results a curved facet as shown in Fig. 7.21. It is helpful to predict the effect of such facet on a laser/light emitter far-field pattern. A simple model was created to approximate such morphology. The curved facet can be approximated as a cylindrical cut specified with a starting angle θ_1 , ending

angle θ_2 and a radius R . Now, let's assume the light propagates (Light propagates through multiple reflection inside a waveguide.) within an angular limit ϕ_1 and ϕ_2 . Using Monte-Carlo method, one can trace individual beams and perform a segmented sum over a given viewing angle. The algorithm is as follows:

- 1) Pick a random exit point on the facet.
- 2) Choose a random (either uniform or specific distribution) direction within the angular limits.
- 3) Calculate the refracted angle θ_x with respect to x -axis
- 4) Increment the segmented sum within $\theta < \theta_x < \theta + \Delta\theta$ by $+1$
- 5) Repeat Step 1

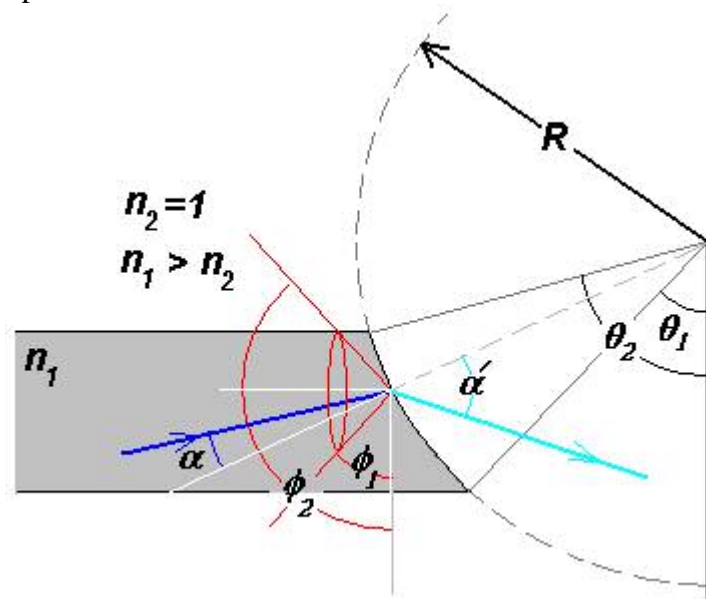
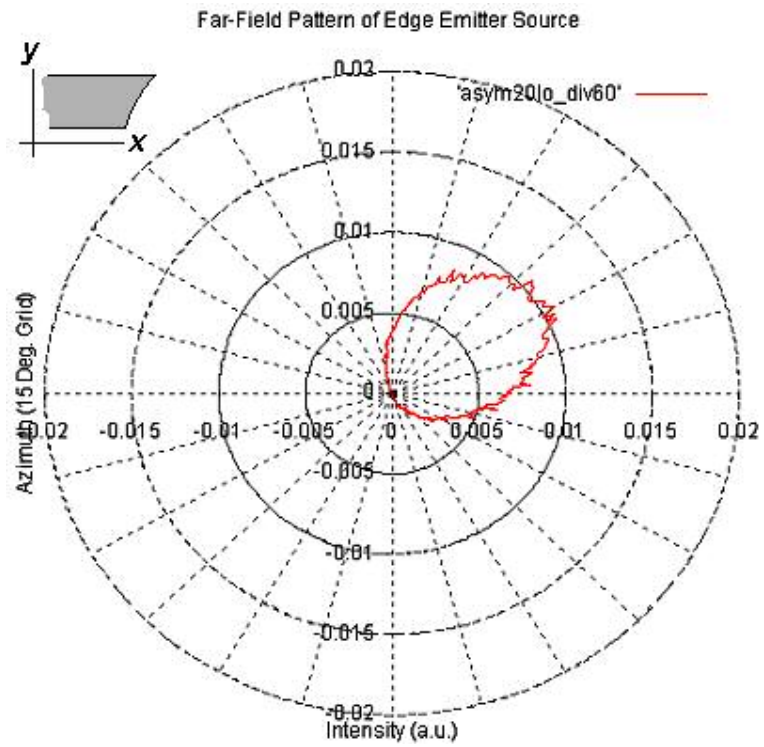
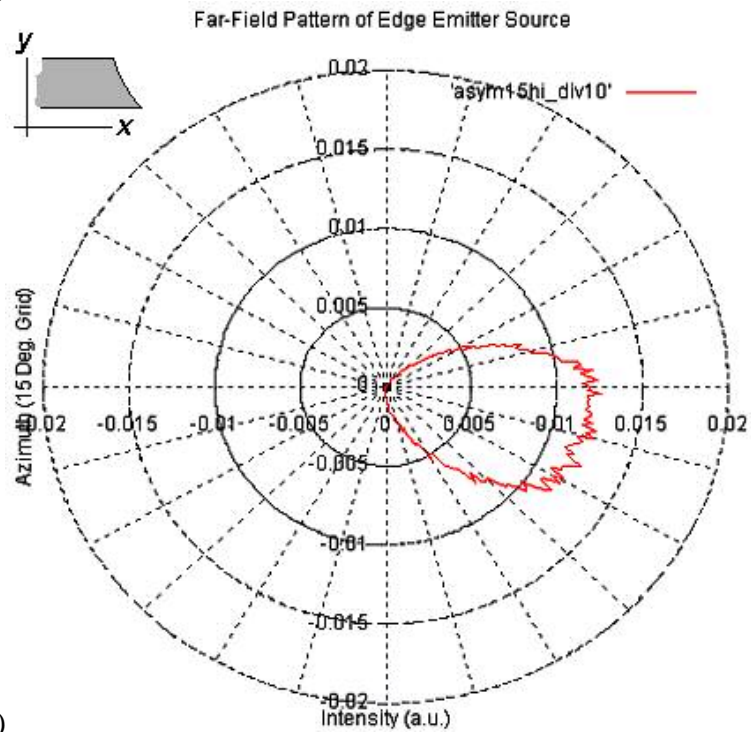


Fig. 7.21) A geometric model of an etched facet



a)



b)

Fig. 7.22 (a) Asymmetric face-down facet (20° facet, 60° angular limit),
 (b) Asymmetric face-up facet (15° facet, 10° angular limit)

7.3.3 VCSEL Reflectivity/Transmission Spectrum

Dielectric mirrors (DBR) play a crucial role in VCSEL design. As discussed in chapter 1 a practical DBR consists of several quarter wavelength paired layers. In order to simulate the spectral response of a DBR stack, transfer matrix can be used to determine the electric and magnetic field intensity. The transfer matrix for a single layer can be written as^{xxvii}

$$M = \begin{bmatrix} \cos(kd) & \frac{-j}{n} \sin(kd) \\ -jn \sin(kd) & \cos(kd) \end{bmatrix} \quad (7.5)$$

where K is wave vector, j is imaginary unit, n is refractive index and d is thickness. For N different layers we can rewrite Eq. 7.5 as

$$M_{Layers} = \prod_{i=1}^N \begin{bmatrix} \cos(k_i d_i) & \frac{-j}{n_i} \sin(k_i d_i) \\ -jn_i \sin(k_i d_i) & \cos(k_i d_i) \end{bmatrix} = \begin{bmatrix} A & B \\ C & D \end{bmatrix} \quad (7.6)$$

The reflection r and transmission t coefficients can then be written

$$r = \frac{An_0 + Bn_T n_0 - C - Dn_T}{An_0 + Bn_T n_0 + C + Dn_T} \quad (7.7)$$

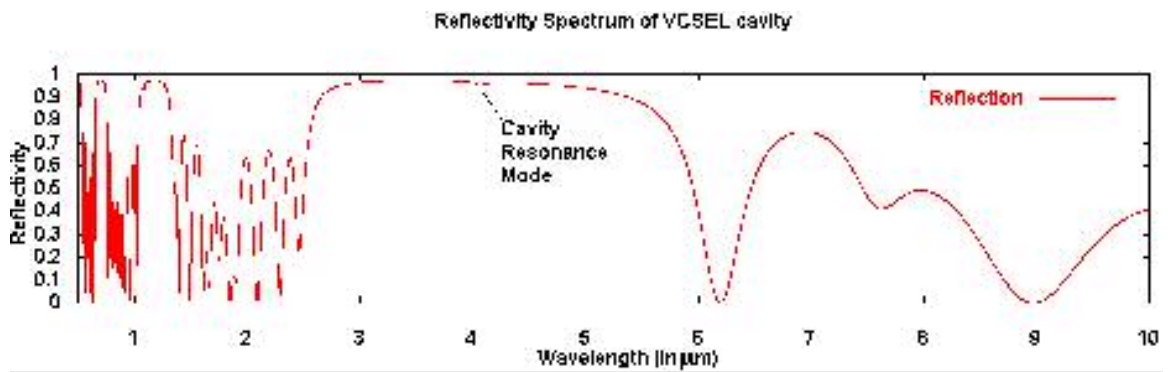
$$t = \frac{2n_0}{An_0 + Bn_T n_0 + C + Dn_T} \quad (7.8)$$

where n_0 and n_T are the refracting of the initial and final mediums respectively. The reflectance R and transmittance T are given by

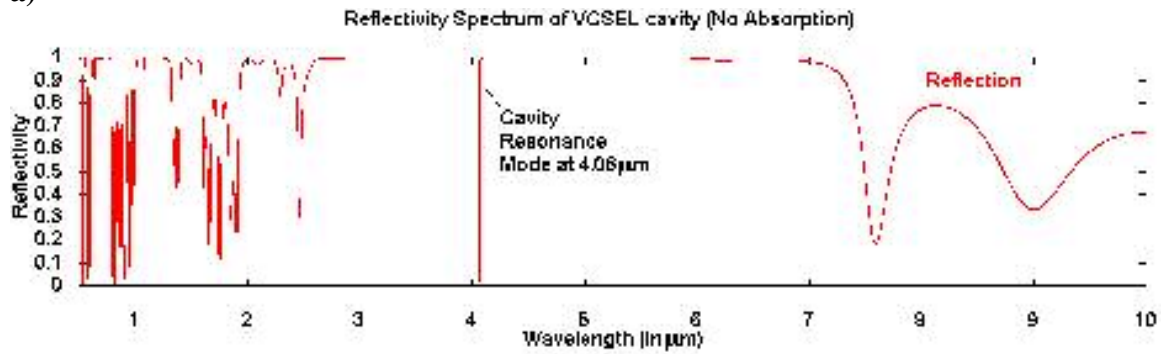
$$R = r \cdot r^* \text{ and } T = t \cdot t^* \quad (7.9)$$

By using a complex value for refractive index, absorption can then be included in Eq. 7.6.

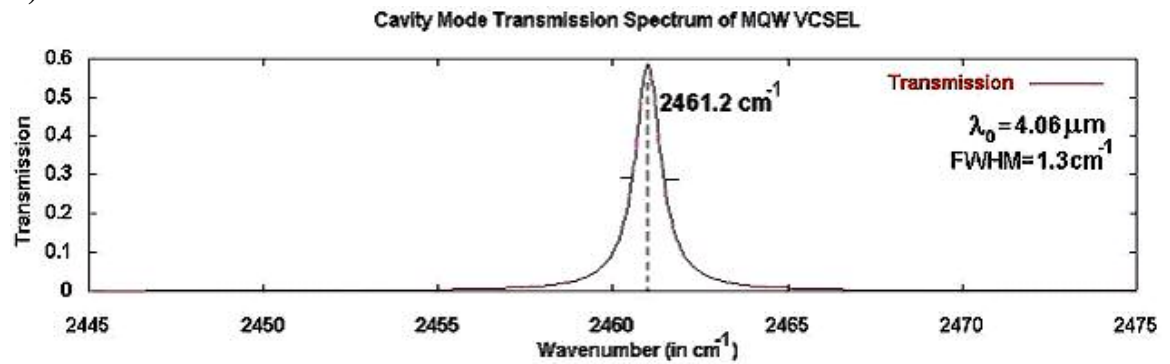
Fig. 7.23 shows the result of this simulation for a VCSEL sample^{xxvii}.



a)



b)



c)

Fig. 7.23) (a) Reflectivity Spectrum of VCSEL cavity with and (b) without absorption
(c) High resolution Cavity Transmission mode without absorption

REFERENCES: